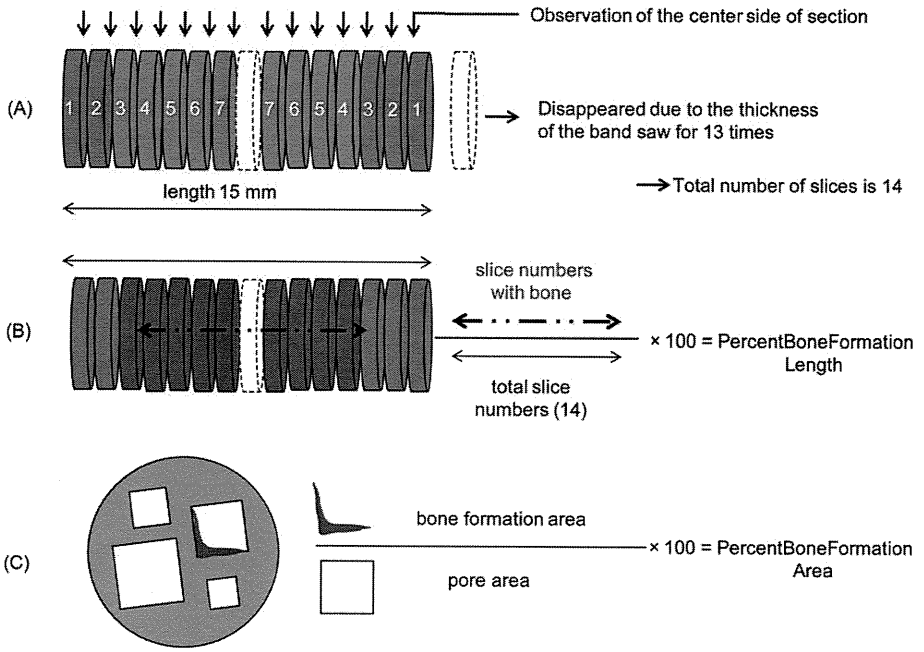

Fig. 2. Schema of the assessment procedure. (A) Detailed method for preparing the 1 mm slice section. (B) Percent bone formation length was calculated as the percentage of slices with bone from among the total 14 slices. Red slices indicate slices with osteoinduction. (C) Percent bone formation area is the percentage of pore area covered in new bone.

Table 1
Comparison of the design and measured dimensions of 10 samples fabricated by selective laser melting.

	Diameter (mm)	Height (mm)	Diagonal length (μm)			
Design value	3.3	15	500	600	900	1200
Measured value	3.20 ± 0.077	15.05 ± 0.2	523.67 ± 36.82	636.87 ± 27.27	947.63 ± 43.88	1264.73 ± 23.42

actual diagonal widths were 524 ± 37, 637 ± 27, 948 ± 44, and 1265 ± 23 μm for p500, p600, p900, and p1200, respectively. The percentage errors were 4.73%, 6.14%, 5.29%, and 5.39%, respectively – 3.03% for an outer diameter of 3.3 mm and 0.31% for a shaft length of 15 mm.

Fig. 1C and D shows micro-CT images of a channel implant fabricated by SLM. The dimensions and internal structure have been faithfully reproduced in accordance with the CAD design. In addition, the external and internal surfaces were observed to form rough structures, such as rugae, on heat treatment at 1300 °C after the SLM treatment. Fig. 1E shows SEM images of a p500 implant which had been divided into two using pliers. The rough structure has the appearance of rugae with a uniform microporous structure on each channel surface.

3.1.2. Surface morphology before implantation

The SEM figures showed that the channel wall surfaces of the untreated channel implants were smooth (Fig. 3A). In contrast, a fine nanosized network structure was observed on the outer surface and on every channel wall surface of the central portion (Fig. 3B and C) of the treated samples. In this manner the SEM figures revealed that in the bioactive channel implants the chemical and thermal treatments successfully penetrated the implant core.

3.1.3. Assessment of in vitro apatite forming ability

After the divided channel implants had been soaked in SBF apatite particles were deposited over the entire surface within 3 days in every channel (Fig. 3D); this indicates that the channel implants possess a homogeneous bioactive surface layer throughout the inner channels of the implant. On the other hand, no surface morphological changes or apatite deposits were observed in the untreated channel implants after soaking in SBF for 7 days.

3.2. In vivo evaluation

3.2.1. Gross inspection

All the dogs tolerated the operation well. No infections at the operative site or implant dislocations were observed in the operative field. All the implants were stable at all post-implantation time points. No apparent adverse reactions such as inflammation or foreign body reactions were noted on or around any of the implants.

3.2.2. Histological findings

Within 16 weeks osteoinduction was observed in all the channels of all treated implants. New bone formed as excellent laminated bone along the channel wall surface. Considerably more bone quantity was observed in p500 and p600 than in p900 and p1200. No bone formation could be recognized on the outer surfaces of the bioactive, treated implants, and no crystal formation or pathological calcification was observed. There was no sign of cartilage formation or endochondral ossification. In contrast, no bone formation was detected in any of the untreated implants at all post-implantation times. They were filled with fibrous tissue containing capillaries.

At 26 and 52 weeks (Fig. 4) new bone was observed as more thickly laminated bone along the channel wall surface than at 16 weeks. Hence, the amount of new bone formation clearly increased with time. In a magnified section (Fig. 5) obvious bone

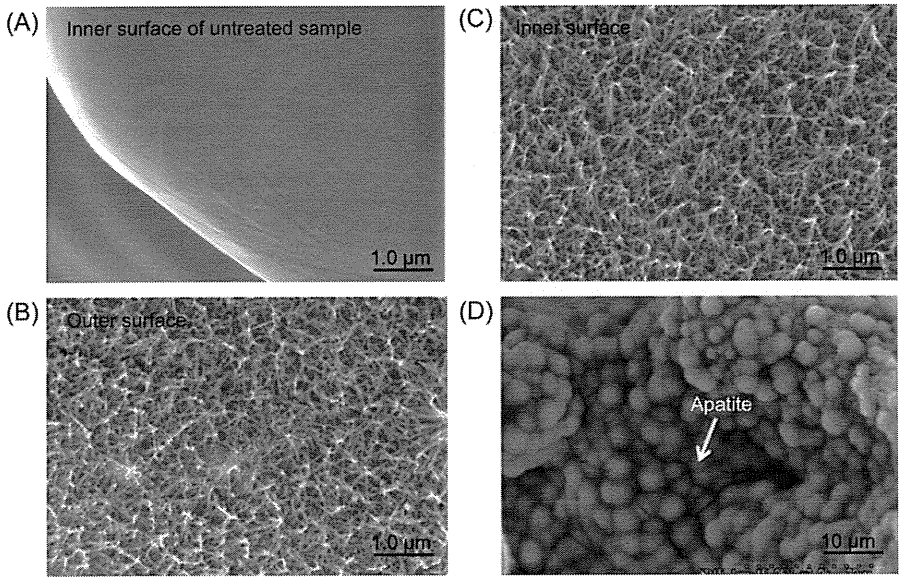

Fig. 3. (A–C) FE-SEM pictures of the outer and inner surface of implant p500. (A) Inner surface of an untreated p500 implant. (B) Outer surface and (C) inner surface of a treated p500 implant. (D) FE-SEM photographs of the surfaces of a treated p500 implant after immersion in SBF for 3 days. Apatite formation on the surface can be seen.

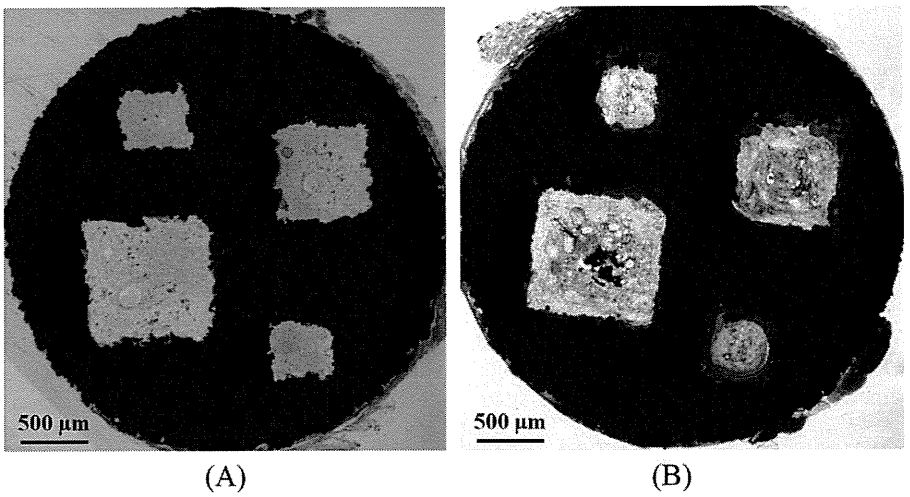

Fig. 4. Non-decalcified histological sections 5 mm from the near end of the untreated and bioactive treated implants at 26 weeks observed by transmitted light microscopy. (A) No bone formation was detected in any untreated implants. (B) Induction of new bone was observed in all pores of treated implants. Stevenel's blue and Van Gieson's picrofuchsin staining. Red color denotes bone.

formation with osteocytes containing blue stained nuclei lined with cuboidal osteoblast-like cells can be seen.

New bone formed on the implant channel surface and bonded directly, as seen in the backscattered SEM image (Fig. 6A). Bony structure (lamella bone with osteocytes) was clearly observed in the backscattered SEM scan. EDX analysis indicated that this bony tissue included calcium and phosphorous with a Ca/P ratio of 1.67 wt.%.

3.2.3. Bone formation length (Fig. 7)

At 16, 26, and 52 weeks the PBFL values for the bioactive implants were 52 ± 12, 54 ± 12, 35 ± 15, and 29 ± 18, 66 ± 8.6, 69 ± 18, 45 ± 20, and 46 ± 17, and 81 ± 14, 74 ± 9, 68 ± 11, and 65 ± 17, respectively, for p500, p600, p900, and p1200, respectively. Furthermore, in the relatively early post-implantation period the PBFL was significantly greater in p500 and p600 than in p900 and p1200. The PBFL for the untreated implants was 0 from 16 to 52 weeks because no bone was observed in any channel.

3.2.4. Total induced bone volume (Fig. 8)

At 16, 26, and 52 weeks the TIBV values for the bioactive implants were 0.17 ± 0.13, 0.26 ± 0.14, 0.23 ± 0.14, and 0.21 ± 0.16, 0.37 ± 0.21, 0.44 ± 0.28, 0.33 ± 0.30, and 0.45 ± 0.43, and 0.51 ± 0.26, 0.57 ± 0.30, 0.80 ± 0.60, and 0.92 ± 0.84, respectively, for p500, p600, p900, and p1200, respectively. As the channel size increased the TIBV increased at 52 weeks, however, the volume did not change significantly with time. Of course, TIBV for the untreated implants was 0 at 52 weeks.

3.2.5. Average bone formation area (Fig. 9)

At 16, 26, and 52 weeks, the average PBFA values for the bioactive implants were 8.4 ± 6.3, 8.5 ± 4.6, 3.4 ± 2.1, and 1.8 ± 1.4, 18.2 ± 10.4, 14.5 ± 9.3, 4.9 ± 4.5, and 3.7 ± 3.6, and 25.0 ± 12.7, 18.7 ± 9.9, 11.8 ± 9.0, and 7.6 ± 7.0, respectively, for p500, p600, p900 and p1200, respectively. The average PBFA in p500 was the greatest at every time point. Hence, the bone formation area was significantly greater in smaller channels at all time points. In

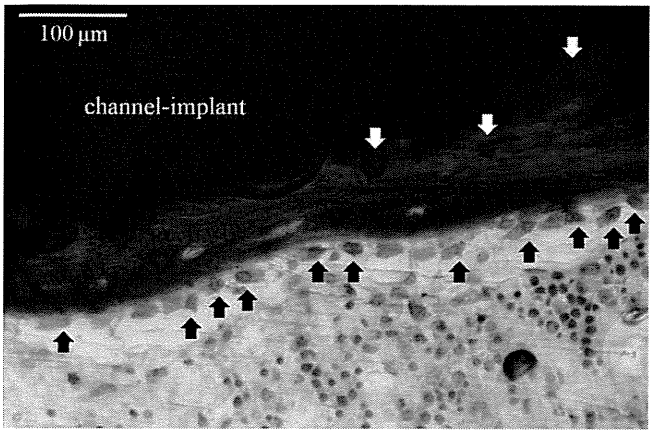

Fig. 5. Magnification of the non-decalcified histological sections 5 mm from the near end of the treated implants at 26 weeks observed by transmitted light microscopy. Obvious bone formation with osteocytes (white arrow) containing blue stained nuclei can be seen. Osteoblast-like cells (black arrow) can be seen as an osteoid-like tissue layer. Stevenel's blue and Van Gieson's picrofuchsin staining. Red color denotes bone.

addition, this tendency for the average bone formation area was similar to that for the bone formation length rate at all time points. The average PBFA for the untreated implant was 0 for all channel sizes at 52 weeks.

3.2.6. Distribution of PBFA

Fig. 10A shows the relationship between PBFA and its location in each channel at 16 weeks. A point 5 mm from the near end represents the peak of the line graph for PBFA in p500 and p600. The line graphs for p900 and p1200 are gentle curves. The peak values of the line graphs for p500 and p600 were higher than those for p900 and p1200.

At 26 weeks the peaks of the line graphs for PBFA in p500 and p600 are somewhat gentle, with a central focus at 5 mm (Fig. 10B). PBFA for p900 and p1200 were high closer to the center of the implants. The peak values of the line graphs for p500 and p600 were higher than those for p900 and p1200, similar to the results for 16 weeks.

At 52 weeks the curves of the line graphs for PBFA are gentler and higher than those at 26 weeks (Fig. 10C). The curves of the line graphs for p500 and p600 were consistently higher than those for p900 and p1200 at 52 weeks.

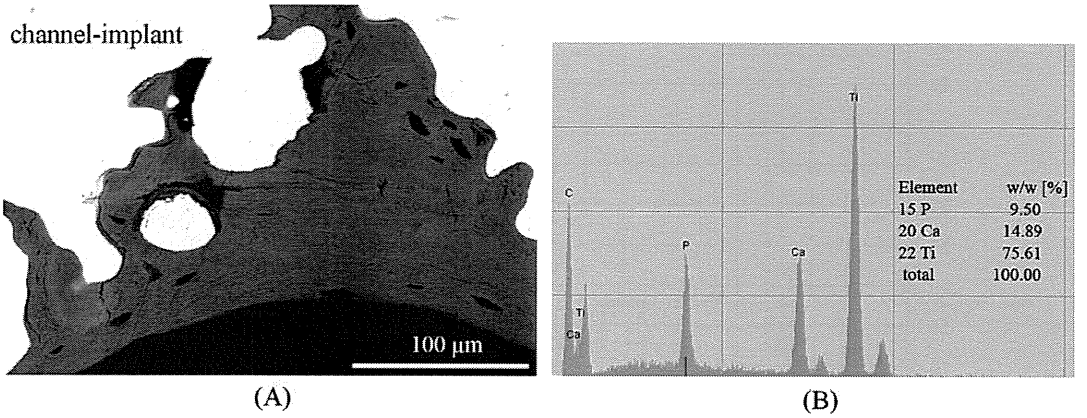

Fig. 6. (A) Backscattered SEM image 5 mm from the near end of the treated implants at 26 weeks. New bone has formed on the channel implant surface and has bonded directly. (B) EDX analysis of the newly formed bone. The bony structure contained calcium and phosphorous; the Ca/P ratio was 1.67 wt.%.

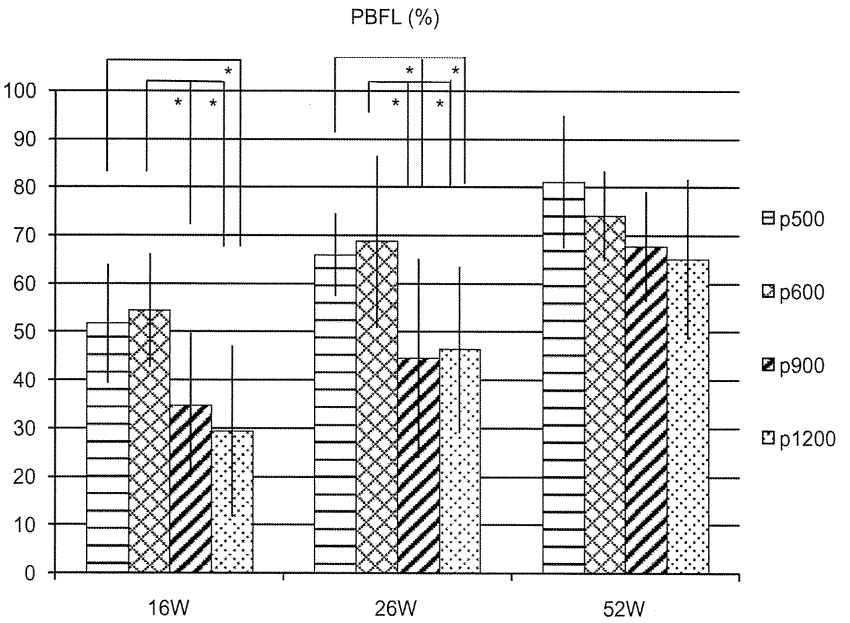

Fig. 7. Histomorphometric results for PBFL at each post-implantation time. In the relatively early post-implantation period PBFL was significantly greater in p500 and p600 than in p900 and p1200. * Denotes significant difference.

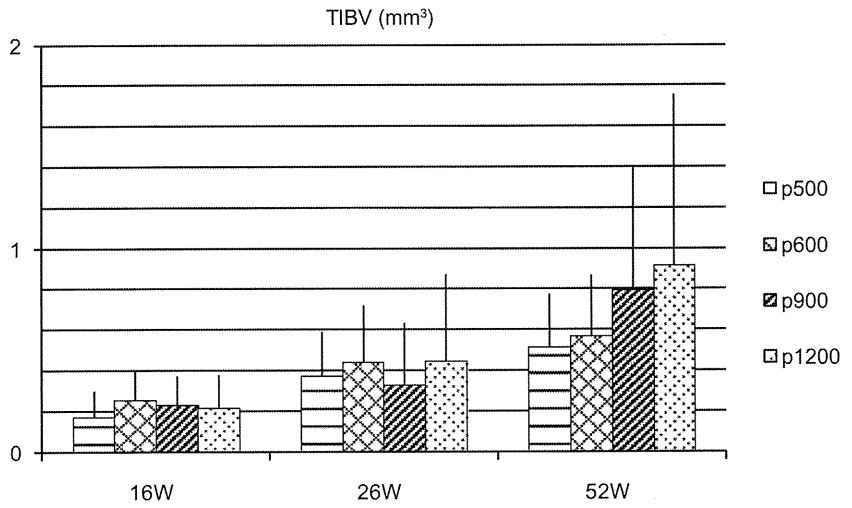

Fig. 8. Histomorphometric results for TIBV at each post-implantation time. As pore size increased TIBV at 52 weeks became greater. However, there was no significant difference for any period ($P < 0.05$).

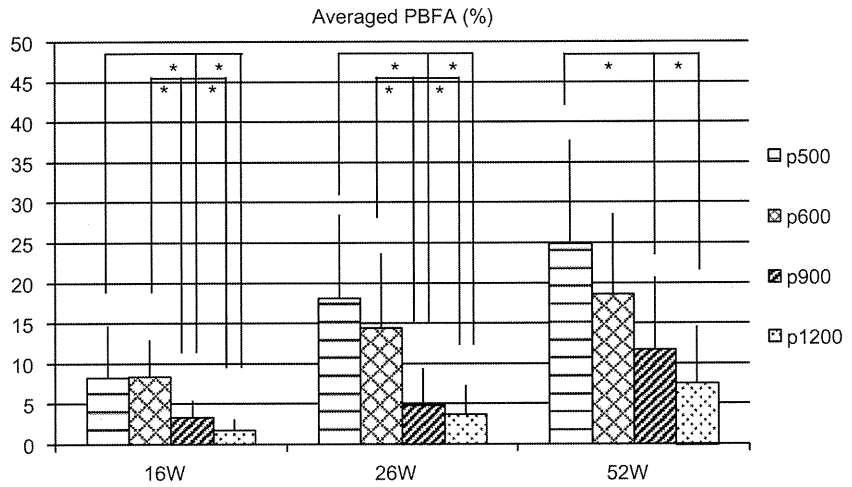

Fig. 9. Histomorphometric results for averaged PBFA at each post-implantation time. Averaged PBFA in p500 was significantly greater than that in p900 or p1200 at all time points ($P < 0.05$). * Denotes significant difference.

4. Discussion

To our knowledge this report presents the first definitive comparison of in vivo osteoinductivity with different interconnective pore sizes (p500, p600, p900, and p1200) of identical implants in identical environments. In addition, we evaluated the location and quantity of bone formed and variations the time-course of formation in each interconnective pore by sectioning each specimen (every 1 mm) after 16, 26, and 52 weeks implantation. These investigations were made possible by the development of our channel implants, whose macrostructure could be controlled by the RP-based SLM technique. Simultaneously, the preparation of homogeneous microstructures and nanostructures by heat treatment at 1300 °C and subsequent chemical and thermal treatment also played an important part in the present experiment. Significant osteoinduction was observed in p500 and p600. Furthermore, we found that the greatest osteoinduction in the early period occurred 5 mm from both ends of the implants in p500 and p600.

A high magnification view of non-decalcified histological sections (Fig. 5) clearly demonstrates obvious bone formation with an osteocyte layer containing blue stained nuclei lined with osteoblast-like cells. When observed by backscattered SEM and analyzed using SEM-EDX it had the structure of lamella bone with osteocytes and had a Ca/P ratio of 1.67. These findings strongly indicate that this bony structure is newly formed bone tissue and not crystal formation or pathological calcification.

Kruyt et al. employed comparative models with different pore sizes and reported that rough HA samples with pores of 800 μm were significantly better than smooth samples having pores of 600 μm with respect to bone formation inside the pores in vivo [32]. Yuan et al. reported that, for almost the same chemical constitution, HA rods with an average pore size of 200 μm and smooth and dense pore walls failed to induce ectopic bone formation, whereas rods with an average pore size of 400 μm and rough and porous pore walls were successful [33]. However, these reports are not accurate comparisons of the pore size because the surface structures of the materials were different. Moreover, it has also been speculated that the degree of interconnectivity of porous scaffolds is more significant than the pore size in the case of vascular networks requiring new bone penetration, and formation is chiefly influenced by the interconnectivity [34]. As a result, simple channel implants such as those in the present study were required to identify the definite effects of interconnective pore size on osteoinduction. The present study has shown that a relationship

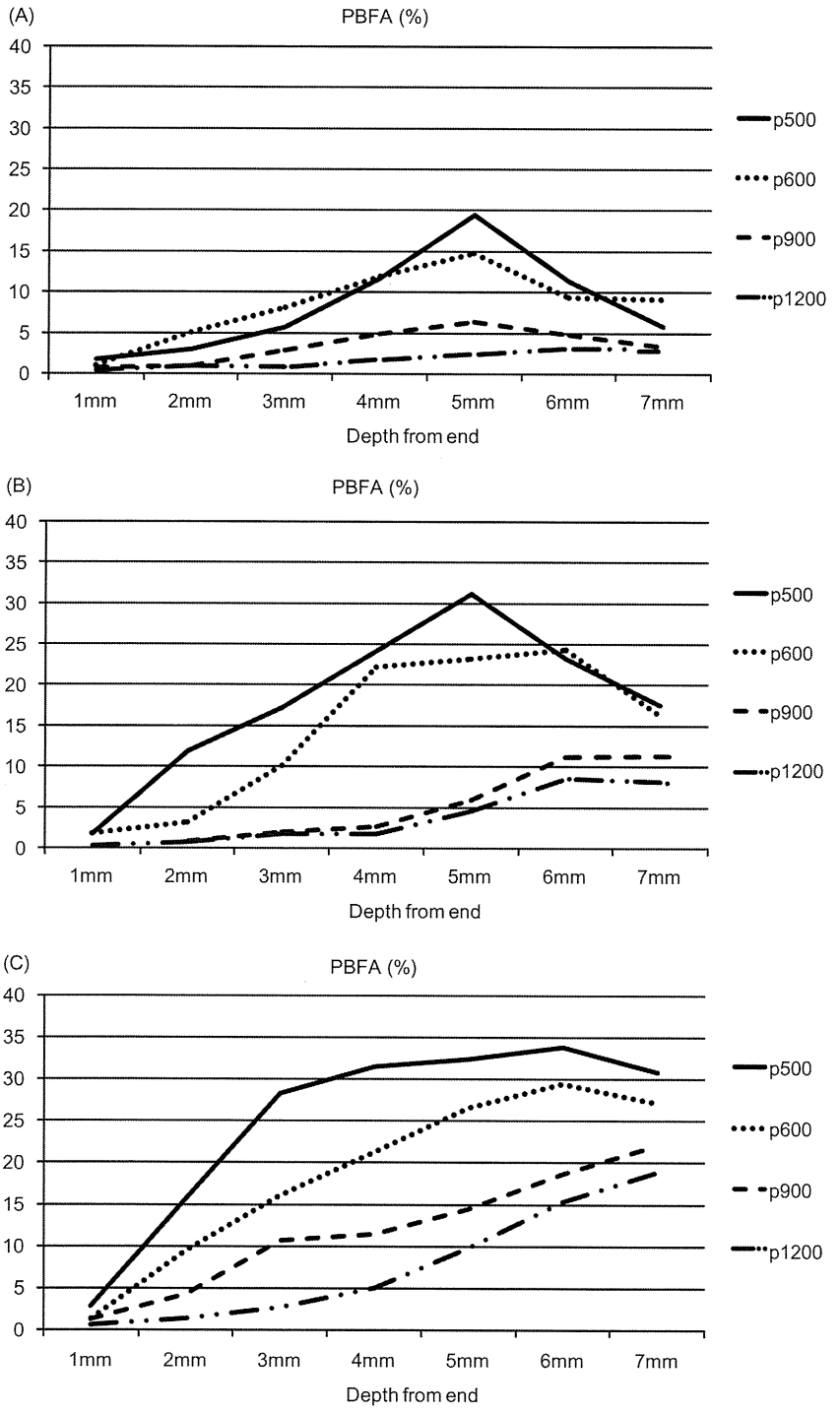

Fig. 10. (A) Location of PBFA of each pore at 16 weeks. A point 5 mm from the near end was the peak of the line graph for PBFA in p500 and p600. Overall, the line graphs in p900 and p1200 formed a low peak. (B) Location of PBFA of each pore at 26 weeks. The peak of the line graph for PBFA in p500 and p600 became gentle with a central focus at 5 mm. (C) Location of PBFA of each pore at 52 weeks. The curve of the line graph of PBFA at 52 weeks became gentler than that at 26 weeks. The peak values for p500 and p600 were higher than those for p900 and p1200 at all locations.

exists between osteoinduction and interconnection size in the range 500–1200 μm.

In terms of the average PBFA, p500 was significantly different from p900 and p1200 at every implantation time point. In terms of PBFL, which is a measure of bone spread, there were significant differences between p500 and both p900 and p1200 and between p600 and both p900 and p1200 at 26 weeks. TIBV showed a tendency to increase with increasing channel size at 52 weeks. However, significant differences were not observed. In general, the fraction of total pore area available for bone formation (average PBFA) is used to evaluate bone formation in the porous body [12,35]. Hence, in studies on porous biomaterials an increase in the ratio of TIBV to total pore volume is a good indicator of improved osteoinductivity. Therefore, of our channel implants we consider p500 (diagonal width 500 μm), which had highest bone area fraction, to be the most osteoinductive, regardless of the implantation period.

In the case of p500 it appears that the concentrations of calcium and phosphate ions could easily reach supersaturation levels, in

contrast to the other channel sizes, because it is smallest. On the other hand, no bone formation could be recognized on the outer surface of the treated channel implants or in any untreated implants at 52 weeks; these results coincide with the consensus that chemical composition, macropores, and poor shear stresses are important for osteoinduction in biomaterials [10,36,37].

In the present study we also evaluated variations in the location, quantity, and time-course of the bone formed in each pore size. These results are represented in terms of the distance from the end (Fig. 10). In the case of p500 and p600 at 16 weeks it appears that osteoinduction might occur at approximately 5 mm from both ends (one-third of the total length). At 26 weeks excellent osteoinduction was observed at distances of 4, 5, and 6 mm from both ends in p500 and p600. We consider that the increasing bone quantity in this region results in it spreading from a point 5 mm distant from both ends. At 52 weeks further excellent osteoinduction was observed at distances of 3–7 mm from both ends of p500. The spread occupied more than two-thirds of the total implant length. In p900 and p1200 the PBFA was better near the implant center than near the ends at 26 weeks, and bone spread was not observed. It appeared that it was particularly difficult for bone formation to spread towards the end of the implant in the large pores. Therefore, we consider that a certain distance from the end is necessary for each pore in accordance with its pore size. In conventional experiments osteoinduction was found to occur only 2.5–3 mm from the implant periphery because the implant itself was 5–6 mm in diameter [8,10,12,35]. In the present study we used channel implants that were 15 mm in length and found that the greatest osteoinduction occurred 5 mm from the periphery in implants with an interconnective pore size of 500–600 μm and at 7 mm from the periphery in pores of size 900–1200 μm. These results suggest that a wider pore throat might be necessary for larger implants.

The mechanism of osteoinduction in porous biomaterials and its biological effects are still largely unknown. However, it has been elucidated that biomaterials must meet very specific requirements in terms of macrostructure, microstructure, and chemical composition in order to be osteoinductive [36]. In terms of macrostructure, Habibovic et al. reported that the pores in interconnected porous structures are an important feature because they provide a protected area without strong fluid movement, thereby giving the cells sufficient space to differentiate along the osteogenic lineage [38]. Our finding that p500 and p600 are more osteoinductive than p900 and p1200 and that in p900 and p1200 osteoinduction occurred deeper in the pores supports their arguments. Besides this physiological theory, the protected pore area in narrow or deep pores has a further advantage with respect to non-susceptibility to myogenic or fibrogenic factors from the surrounding tissue. Kruyt et al. also discussed the importance of a protected pore area for osteoinduction and speculated that the concentrations of calcium and phosphate ions reaches supersaturation levels in the vicinity [37].

In addition, the fact that in p500 and p600 osteoinduction mainly occurred at 5 mm rather than at more distant locations indicates that, to some extent, osteoinduction is influenced by diffusion factors or vascularization or tissue invasion. Kuboki et al. reported that in a bone morphogenetic protein (BMP)-induced osteogenesis model, when blood supply is sufficient such that oxygen and nutrient levels are ample, direct osteogenesis occurred, whereas with lesser vasculature chondrogenesis occurred [39]. In material-induced osteoinduction bone formation is always via direct osteogenesis, indicating that osteoinduction occurs in the presence of a sufficient blood supply; in this respect, peripherals area are more favorable. Thus, as shown in the present study, a distance of 5 mm may represent the optimum balance between vasculature, the availability of calcium and phosphate ions, and fluid movement in the case of p500 and p600. This argument is also consistent with the fact that no bone formation could be seen on the outer surfaces of the treated implants and there was no pore throat occluded by bone anywhere along its length.

For the same reasons, no bone formation could be seen on the outer surfaces of treated p900 and p1200 implants and bone formation tended to occur deeper in the pores. Similarly, there was no pore throat occluded by bone anywhere along its length. These results are consistent with the fact that osteoinduction does not occur in the peripheral pores of a porous implant [12,37].

It appears that the results of the present study represent the initial stages in our understanding of the character and mechanism of osteoinduction in terms of the relationship between osteoinduction and interconnective pore size. Final conclusions can be obtained only by investigating pore sizes smaller than 500 μm and lengths greater than 15 mm. As mentioned previously, the mechanisms responsible for osteoinduction by biomaterials and their biological effects are still largely unknown.

Many reports have discussed the accuracy of reproduction possible with RP techniques [40,41]; the dimensional errors in the present study are approximately identical to values previously reported. However, some issues are still to be resolved, in particular, compared with the design value the measured pore sizes are larger and the outer diameters of the implants are smaller, whereas the implant length is the same. Significant effort is needed to solve these problems and improve precision.

One weakness of the present study concerns only the use of pores wider than 500 μm due to manufacturing limitations. However, we consider that new knowledge has been obtained, as the optimal pore size for osteoinduction has not previously been explored. Investigations of pore sizes less than 500 μm remain a pending issue.

5. Conclusion

The architecture of channel implants whose macrostructure could be controlled by the RP-based SLM technique was very effective for investigating and evaluating the influence of interconnective pore size on osteoinduction. The chemically and heat-treated channel implants exhibited better osteoinductivity and induced ectopic bone growth in the back muscles of beagle dogs within 16 weeks. The resulting bone formation area and length suggested excellent osteoinduction in the case of a 500 μm pore size within the range 500–1200 μm. Furthermore, the highest osteoinduction value in the early periods was observed at a distance of 5 mm from both ends of the implants when the pore size was approximately 500 μm. Further investigations of suitable pore sizes for osteoinduction are necessary for pore sizes less than 500 μm.

Acknowledgements

This work was supported by the Translational Research Promotion Project of the Health Assurance Program of the New Energy and Industrial Technology Development Organization (NEDO).

Appendix A. Figures with essential colour discrimination

Certain figures in this article, particularly Figures 1, 2, 4–6, are difficult to interpret in black and white. The full colour images can be found in the on-line version, at doi: 10.1016/j.actbio.2011.01.036

References

[1] Hench L, Wilson J. Introduction to bioceramics. Singapore: World Scientific; 1993.
[2] Yang Z, Yuan H, Tong W, Zou P, Chen W, Zhang X. Osteogenesis in extraskeletally implanted porous calcium phosphate ceramics: variability among different kinds of animals. Biomaterials 1996;17:2131–7.

[3] Yuan H et al. Bone formation induced by calcium phosphate ceramics in soft tissue of dogs: a comparative study between porous alpha-TCP and beta-TCP. J Mater Sci 2001;12:7–13.
[4] Yuan H, de Bruijn JD, Zhang X, van Blitterswijk CA, de Groot K. Bone induction by porous glass ceramic made from bioglass (45S5). J Biomed Mater Res 2001;58:270–6.
[5] Yamasaki H, Sakai H. Osteogenic response to porous hydroxyapatite ceramics under the skin of dogs. Biomaterials 1992;13:308–12.
[6] Ripamonti U. The morphogenesis of bone in replicas of porous hydroxyapatite obtained from conversion of calcium carbonate exoskeletons of coral. J Bone Joint Surg 1991;73:692–703.
[7] Yuan H, Yang Z, Li Y, Zhang X, De Bruijn JD, De Groot K. Osteoinduction by calcium phosphate biomaterials. J Mater Sci 1998;9:723–6.
[8] Habibovic P et al. Biological performance of uncoated and octacalcium phosphate-coated Ti6Al4V. Biomaterials 2005;26:23–36.
[9] Barrere F et al. Osteogenecity of octacalcium phosphate coatings applied on porous metal implants. J Biomed Mater Res A 2003;66:779–88.
[10] Fujibayashi S, Neo M, Kim HM, Kokubo T, Nakamura T. Osteoinduction of porous bioactive titanium metal. Biomaterials 2004;25:443–50.
[11] Cheng L et al. Osteoinduction of hydroxyapatite/beta-tricalcium phosphate bioceramics in mice with a fractured fibula. Acta Biomater 2010;6:1569–74.
[12] Takemoto M et al. Osteoinductive porous titanium implants: effect of sodium removal by dilute HCl treatment. Biomaterials 2006;27:2682–91.
[13] Habibovic P, Yuan H, van den Doel M, Sees TM, van Blitterswijk CA, de Groot K. Relevance of osteoinductive biomaterials in critical-sized orthotopic defect. J Orthop Res 2006;24:867–76.
[14] Habibovic P, Gbureck U, Doillon CJ, Bassett DC, van Blitterswijk CA, Barralet JE. Osteoconduction and osteoinduction of low-temperature 3D printed bioceramic implants. Biomaterials 2008;29:944–53.
[15] Takemoto M, Fujibayashi S, Akiyama N, Matsushita T, Kokubo T, Nakamura T. Effect of pore structure on osteoconductivity and osteoinductivity of porous bioactive titanium. In: Transactions of the 8th world biomaterials congress. Amsterdam, Netherlands: Curran Associates; 2008.
[16] Habibovic P et al. Comparative in vivo study of six hydroxyapatite-based bone graft substitutes. J Orthop Res 2008;26:1363–70.
[17] Yuan H, van Blitterswijk CA, de Groot K, de Bruijn JD. A comparison of bone formation in biphasic calcium phosphate (BCP) and hydroxyapatite (HA) implanted in muscle and bone of dogs at different time periods. J Biomed Mater Res A 2006;78:139–47.
[18] Ye F et al. A long-term evaluation of osteoinductive HA/beta-TCP ceramics in vivo: 4.5 years study in pigs. J Mater Sci 2007;18:2173–8.
[19] Kondo N et al. Osteoinduction with highly purified beta-tricalcium phosphate in dog dorsal muscles and the proliferation of osteoclasts before heterotopic bone formation. Biomaterials 2006;27:4419–27.
[20] Lin CY, Wirtz T, LaMarca F, Hollister SJ. Structural and mechanical evaluations of a topology optimized titanium interbody fusion cage fabricated by selective laser melting process. J Biomed Mater Res A 2007;83:272–9.
[21] Mullen L, Stamp RC, Fox P, Jones E, Ngo C, Sutcliffe CJ. Selective laser melting: a unit cell approach for the manufacture of porous, titanium, bone in-growth constructs, suitable for orthopedic applications. II. Randomized structures. J Biomed Mater Res B Appl Biomater 2010;92:178–88.
[22] Warnke PH et al. Rapid prototyping: porous titanium alloy scaffolds produced by selective laser melting for bone tissue engineering. Tissue Eng C 2009;15:115–24.
[23] Pattanayak DK, et al. Fabrication of bioactive porous Ti metal with structure similar to human cancellous bone by selective laser melting. In: Sukyoung K, editor. Bioceramics. Daegu; 2009. p. 163–66.
[24] Frosch KH et al. Growth behavior, matrix production, and gene expression of human osteoblasts in defined cylindrical titanium channels. J Biomed Mater Res A 2004;68:325–34.
[25] Karageorgiou V, Kaplan D. Porosity of 3D biomaterial scaffolds and osteogenesis. Biomaterials 2005;26:5474–91.
[26] Ryan G, Pandit A, Apatsidis DP. Fabrication methods of porous metals for use in orthopaedic applications. Biomaterials 2006;27:2651–70.
[27] Scaglione S, Ilengo C, Fato M, Quarto R. Hydroxyapatite-coated polycaprolactone wide mesh as a model of open structure for bone regeneration. Tissue Eng A 2009;15:155–63.
[28] Pattanayak DK et al. Bioactive Ti metal analogous to human cancellous bone: fabrication by selective laser melting and chemical treatments. Acta Biomater 2011;7(3):1398–406.
[29] Kokubo T, Takadama H. How useful is SBF in predicting in vivo bone bioactivity? Biomaterials 2006;27:2907–15.
[30] Kokubo T, Kushitani H, Sakka S. Solutions able to reproduce in vivo surface-structure changes in bioactive glass-ceramic A-W. J Biomed Mater Res 1990;24:721–34.
[31] Maniatopoulos C, Rodriguez A, Deporter DA, Melcher AH. An improved method for preparing histological sections of metallic implants. Int J Oral Maxillofac Implants 1986;1:31–7.
[32] Kruyt MC, Dhert WJ, Oner C, van Blitterswijk CA, Verbout AJ, de Bruijn JD. Optimization of bone-tissue engineering in goats. J Biomed Mater Res B Appl Biomater 2004;69:113–20.
[33] Yuan H, Kurashina K, de Bruijn JD, Li Y, de Groot K, Zhang X. A preliminary study on osteoinduction of two kinds of calcium phosphate ceramics. Biomaterials 1999;20:1799–806.
[34] Zhao J, Guo LY, Yang XB, Weng J. Preparation of bioactive porous HA/PCL composite scaffolds. Appl Surf Sci 2008;255:2942–6.
[35] Takemoto M, Fujibayashi S, Neo M, Suzuki J, Kokubo T, Nakamura T. Mechanical properties and osteoconductivity of porous bioactive titanium. Biomaterials 2005;26:6014–23.
[36] Habibovic P, de Groot K. Osteoinductive biomaterials – properties and relevance in bone repair. J Tissue Eng Regen Med 2007;1:25–32.
[37] Kruyt MC et al. Optimization of bone tissue engineering in goats: a peroperative seeding method using cryopreserved cells and localized bone formation in calcium phosphate scaffolds. Transplantation 2004;77:359–65.
[38] Habibovic P, van der Valk CM, van Blitterswijk CA, De Groot K, Meijer G. Influence of octacalcium phosphate coating on osteoinductive properties of biomaterials. J Mater Sci 2004;15:373–80.
[39] Kuboki Y, Jin Q, Takita H. Geometry of carriers controlling phenotypic expression in BMP-induced osteogenesis and chondrogenesis. J Bone Joint Surg 2001;83A(Suppl. 1):S105–15.
[40] Silva DN, Gerhardt de Oliveira M, Meurer E, Meurer MI, Lopes da Silva JV, Santa-Barbara A. Dimensional error in selective laser sintering and 3D-printing of models for craniomaxillary anatomy reconstruction. J Craniomaxillofac Surg 2008;36:443–9.
[41] Ibrahim D et al. Dimensional error of selective laser sintering, three-dimensional printing and PolyJet models in the reproduction of mandibular anatomy. J Craniomaxillofac Surg 2009;37:167–73.

Acta Biomaterialia 7 (2011) 1379–1386

Contents lists available at ScienceDirect

Acta Biomaterialia

journal homepage: www.elsevier.com/locate/actabiomat

Bone bonding bioactivity of Ti metal and Ti–Zr–Nb–Ta alloys with Ca ions incorporated on their surfaces by simple chemical and heat treatments

A. Fukuda [a,*], M. Takemoto [a], T. Saito [a], S. Fujibayashi [a], M. Neo [a], S. Yamaguchi [b], T. Kizuki [b], T. Matsushita [b], M. Niinomi [c], T. Kokubo [b], T. Nakamura [a]

[a] Department of Orthopaedic Surgery, Graduate School of Medicine, Kyoto University, Shogoin, Kawahara-cho 54, Sakyo-ku, Kyoto 606-8507, Japan
[b] Department of Biomedical Sciences, College of Life and Health Sciences, Chubu University, 1200 Matsumoto-cho, Kasugai, Aichi 487-8501, Japan
[c] Department of Biomaterials Science, Institute for Materials Research, Tohoku University, 2-1-1 Katahira, Aoba-ku, Sendai 980-8577, Japan

ARTICLE INFO

Article history:
Received 2 July 2010
Received in revised form 17 September 2010
Accepted 20 September 2010
Available online 29 September 2010

Keywords:
Titanium alloy
Bioactive treatment
Apatite
Bone bonding
In vivo

ABSTRACT

Ti15Zr4Nb4Ta and Ti29Nb13Ta4.6Zr, which do not contain the potentially cytotoxic elements V and Al, represent a new generation of alloys with improved corrosion resistance, mechanical properties, and cytocompatibility. Recently it has become possible for the apatite forming ability of these alloys to be ascertained by treatment with alkali, $CaCl_2$, heat, and water (ACaHW). In order to confirm the actual in vivo bioactivity of commercially pure titanium (cp-Ti) and these alloys after subjecting them to ACaHW treatment at different temperatures, the bone bonding strength of implants made from these materials was evaluated. The failure load between implant and bone was measured for treated and untreated plates at 4, 8, 16, and 26 weeks after implantation in rabbit tibia. The untreated implants showed almost no bonding, whereas all treated implants showed successful bonding by 4 weeks, and the failure load subsequently increased with time. This suggests that a simple and economical ACaHW treatment could successfully be used to impart bone bonding bioactivity to Ti metal and Ti–Zr–Nb–Ta alloys in vivo. In particular, implants heat treated at 700 °C exhibited significantly greater bone bonding strength, as well as augmented in vitro apatite formation, in comparison with those treated at 600 °C. Thus, with this improved bioactive treatment process these advantageous Ti–Zr–Nb–Ta alloys can serve as useful candidates for orthopedic devices.

1. Introduction

Titanium (Ti) and its alloys are the most popular materials for orthopedic and dental implants because of their superior biocompatibility, excellent corrosion resistance, and good mechanical properties. However, they are essentially bioinert materials that, after implantation in the living body, are merely encapsulated by fibrous tissue that isolates them from the surrounding tissue. On the other hand, orthopedic load-bearing devices such as total hip prostheses require direct bonding between living bone and the implant. Hence, various methods have been developed to promote bone in-growth and implant fixation for Ti and its alloys [1,2], including physical modification of the implant design, modification of the surface topography, and chemical modification of the material composition and structure. Among these methods, plasma sprayed hydroxyapatite coating is one of the most extensively investigated methods, and its efficiency has been confirmed by many reports [3,4].

In the past decade we have developed a chemical and heat treatment method to produce bioactive Ti [5–7]. This method can be used to create a long-lasting bioactive layer on the surface of Ti and its alloys, allowing bonding with living bone via a spontaneously formed apatite layer. In this method the implants are simply immersed in aqueous solutions before heat treatment, and the bonding effects extend homogeneously throughout the irregular structure of the implant. This method is considered superior to the conventional hydroxyapatite plasma spray method, wherein the coating tends to be applied to the most superficial areas, thereby resulting in uneven and inadequate treatment. This alkali and heat treatment was applied to a porous commercially pure Ti (cp-Ti) surface layer on an artificial hip prosthesis made of a Ti6Al2Nb1Ta alloy, and its effectiveness was confirmed in clinical trials in Japan [8]. In fact, this bioactive artificial hip joint was approved for clinical use in 2007 (AHFIX, Japan Medical Materials Co., Japan).

We have also reported that our chemical and heat treatment is effective for Ti alloys (Ti6Al4V, Ti15Mo5Zr3Al, and Ti6Al2Nb1Ta) [9–11]. However, these Ti alloys contain aluminum (Al) and vanadium (V), which are suspected of being cytotoxic [12–14]. In this

* Corresponding author. Tel.: +81 75 751 3365; fax: +81 75 751 8409.
E-mail address: akinobu@kuhp.kyoto-u.ac.jp (A. Fukuda).

1742-7061/$ - see front matter © 2010 Acta Materialia Inc. Published by Elsevier Ltd. All rights reserved.
doi:10.1016/j.actbio.2010.09.026

context, the new generation of Ti alloys without V and Al [14], such as Ti15Zr4Ta4Nb and Ti29Nb13Ta4.6Zr, offers a promising alternative. Ti15Zr4Ta4Nb has been reported to show much better corrosion resistance, mechanical properties, and cytocompatibility than Ti6Al4V [15]; furthermore, Ti29Nb13Ta4.6Zr has been reported to show a lower Young's modulus and cytotoxicity than Ti6Al4V and the same cytotoxicity as cp-Ti [14,16]. Unfortunately, these new generation Ti alloys cannot be endowed with in vitro apatite forming ability by conventional chemical and heat treatment.

Instead, we recently found that Ti15Zr4Ta4Nb and Ti29Nb13Ta4.6Zr can be endowed with in vitro apatite forming ability by treatment with NaOH, $CaCl_2$, heat, and water (ACaHW). In vitro examination showed faster and greater apatite formation on the obtained calcium-modified titanate surface in simulated body fluid (SBF), with ion concentrations nearly equal to those of human blood plasma [17,18]. In this treatment calcium hydrogen titanate is formed after treatment of the Ti surface with NaOH and $CaCl_2$. Subsequent heat treatment transforms the calcium hydrogen titanate into calcium titanates and rutile [17,19]. The final water treatment causes a remarkable increase in in vitro apatite forming ability on account of the increasing mobility of the Ca^{2+} ions via incorporation of H_3O^+ ions in the calcium titanate [17]. These results lead us to expect superior in vivo bioactivity when the ACaHW treatment is applied [20]. In the present study, to confirm the in vivo bioactivity of ACaHW-treated cp-Ti, Ti15Zr4Ta4Nb, and Ti29Nb13Ta4.6Zr alloys, the biomechanical performance was investigated by histological examination and tensile strength testing using animal models [21].

2. Materials and methods

2.1. Implant preparation

Plates of size 15 × 10 × 2 mm were prepared from cp-Ti (Ti > 99.5 mass%), Ti15Zr4Ta4Nb (Kobe Steel Ltd.; Ti balance, Zr 14.51, Nb 3.83, Ta 3.94, Pd 0.16, O 0.25 mass%), and Ti29Nb13Ta4.6Zr (Institute for Materials Research, Tohoku University; Ti balance, Nb 28.8, Fe 0.03,Ta 11.7, Zr 4.65, O 0.08, N 0.01, C 0.01 mass%). The plates were polished with a No. 400 diamond plate, then washed with acetone, 2-propanol, and ultrapure water in an ultrasonic cleaner for 30 min each, and finally dried at 40 °C. For bioactivation the plates were first soaked in 10 ml of 5 or 1 M aqueous NaOH solution at 60 °C for 24 h (alkali treatment). After removal from the solution they were gently rinsed with ultrapure water for 30 s and dried at 40 °C. The plates were subsequently soaked in 20 ml of 100 mM $CaCl_2$ solution at 40 °C for 24 h ($CaCl_2$ treatment), and then washed and dried in a similar manner. Next, they were heated to 600 °C (ACaH600 W) or 700 °C (ACaH700 W) at a rate of 5 °C min^{-1} in an electrical furnace in air and kept at that temperature for 1 h, followed by natural cooling. After the heat treatment they were soaked in 20 ml of ultrapure water at 80 °C for 24 h, and then washed and dried (water treatment). The concentrations of NaOH and the temperatures used for the heat treatment are listed in Table 1. In the present study we did not use ACaH600W-treated Ti29Nb13Ta4.6Zr because the Ti29Nb13Ta4.6Zr alloy had not showed apatite forming ability in SBF on ACaH600W treatment in a preliminary study. Untreated plates were used as controls in the animal experiments. Thus, a total of eight different types of plates were implanted.

Table 1
Conditions of treatment with $CaCl_2$, heat, and water after treatment with NaOH.

	Concentration of NaOH solution (60 °C 24 h)	Heat treatment temperature (1 h)
cp-Ti	5 mol l^{-1}	600 °C
	5 mol l^{-1}	700 °C
Ti15Zr4Ta4Nb	5 mol l^{-1}	600 °C
	5 mol l^{-1}	700 °C
Ti29Nb13Ta4.6Zr	1 mol l^{-1}	700 °C

2.2. Surface analyses

The surfaces of the treated plates were analyzed by field emission scanning electron microscopy (FE-SEM) (S-4300, Hitachi Co., Tokyo, Japan) equipped with an energy dispersive X-ray (EDX) analyzer (EMAX-7000, Horiba Ltd., Kyoto, Japan). The FE-SEM and EDX analyses were carried out at accelerating voltages of 15 and 5 keV, respectively.

2.3. Apatite formation in SBF

The apatite forming abilities of the treated plates were examined by soaking them in 48 ml of SBF with ion concentrations (Na^+ 142.0, K^+ 5.0, Ca^{2+} 2.5, Mg^{2+} 1.5, Cl^- 147.8, HCO_3^- 4.2, HPO_4^{2-} 1.0, and SO_4^{2-} 0.5 mM) nearly equal to those of human blood plasma at 36.5 °C [22]. After soaking for 1 or 3 days the plates were removed, gently rinsed with ultrapure water for 30 s, and dried at 40 °C. Apatite formation on their surfaces was examined by FE-SEM and EDX.

2.4. Animal study

The plates were conventionally sterilized using ethylene oxide gas and implanted into the metaphyses of the tibiae of mature male Japanese white rabbits weighing 2.8–3.5 kg. The surgical methods used have been described previously [5,10,21,23]. Briefly, the rabbits were anesthetized with an intravenous injection of sodium pentobarbital (0.5 ml kg^{-1}), an intramuscular injection of ketamine hydrochloride (10 mg kg^{-1}), and local administration of a solution of 1% lidocaine. A 3 cm long longitudinal skin incision was made on the medial side of the knee and the fascia and periosteum were incised and retracted to expose the tibial cortex. Using a dental burr, a 16 × 2 mm^2 hole was made from the medial to the lateral cortex running parallel to the longitudinal axis of the tibial metaphyses, as shown in Fig. 1A. After irrigating the hole with saline, the plates were implanted in the frontal direction, perforating the tibia and protruding from the medial to lateral cortex. The fascia and skin were closed in layers and the same surgical procedures were performed bilaterally.

The animals were housed individually in standard rabbit cages and fed standard rabbit food and water ad libitum. Each rabbit was killed with an overdose of intravenous sodium pentobarbital at 4, 8, 16, and 26 weeks after implantation; a total of 128 rabbits were used (eight plates of each type). The Kyoto University guidelines for animal experiments were observed in this study.

2.5. Measurement of detachment failure load

After death the segments of the proximal tibial metaphyses containing the implanted plates were harvested and prepared for the detachment tests [21]. All samples were kept moist after harvesting. The bone tissue surrounding the plates was carefully removed on both sides and at the ends using a dental burr to remove periosteal bone growth. Traction was applied vertically to the implant surface employing load test equipment (model 1310VRW, Aikoh Engineering Co. Ltd., Nagoya, Japan) at a crosshead speed of 35 mm min^{-1} (Fig. 1B–D). Specially designed hooks held the bone–plate–bone construct. The detachment failure load was measured when the plate detached from the bone. If the plate detached before the test then the failure load was defined as 0 N.

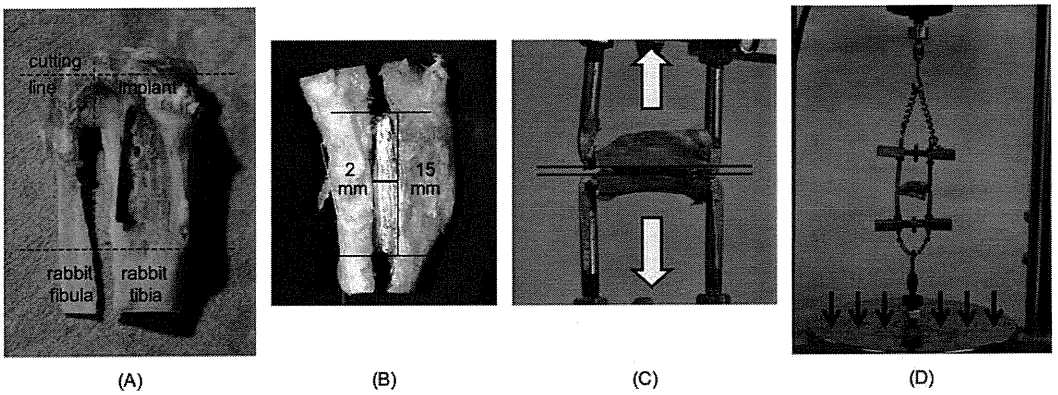

Fig. 1. Photographs of the preparation of rabbit tibia for the detachment test. (A) Insertion of the titanium implant into the tibia (dotted line denotes the cutting line). (B) Detached fragment after cutting the tibia at the proximal and distal ends of the implant. (C) Detachment test. A tensile load is applied by holding the anterior and posterior cortices until detachment. The white arrow indicates the direction of pull. (D) Instron-type autograph. Specially designed hooks held the bone–plate–bone construct. The cross-head speed of the circular disc is 35 mm min^{-1}; the disc moves in the direction of the arrow.

Eight samples were analyzed for each type of implant at each implantation period. All data were recorded as the mean ± standard deviation (SD) and assessed using unpaired one-tailed Student's *t*-test for comparison between untreated and ACaH 700W-treated Ti29Nb13Ta4.6Zr implants at each time point (4, 8, 16, and 26 weeks after implantation), and assessed using one-way analysis of variance (ANOVA) followed by Tukey–Kramer multiple comparison post hoc tests for cp-Ti and Ti15Zr4Ta4Nb at each time point. Differences of $P < 0.05$ were considered statistically significant.

2.6. Histological examination

2.6.1. Surface examination after detachment test

After the detachment tests three samples from each group at each interval after implantation were separated from any soft tissue by soaking in 30% sodium hypochlorite aqueous solution for 3 h. Subsequently they were fixed in 10% phosphate-buffered formalin for 3 days and dehydrated in serial concentrations of ethanol (70, 80, 90, 99, 100, and 100 vol.%) for 1 day each. Then they were soaked in isopentyl acetate solution for 1 day and dried in a critical point drying apparatus (hcp-2, Hitachi Ltd., Tokyo, Japan). The samples were sputter-coated with platinum and palladium for SEM observations (S-4700, Hitachi Ltd., Tokyo, Japan) and coated with carbon for SEM–EDX analyses (EMAX-7000, Horiba Ltd., Kyoto, Japan). The SEM–EDX observations were performed mainly at the sample surface.

2.6.2. Interface examination after detachment test

After the detachment tests five samples from each group at each interval after implantation were fixed in 10% phosphate-buffered formalin for 14 days and dehydrated in serial concentrations of ethanol (70, 80, 90, 99, 100, and 100 vol.%) for 3 days each. Then they were embedded in polyester resin. Sections with thicknesses of 1000 μm were cut using a band saw (BS-3000CP, Exact-Apparatebau, Norderstedt, Germany) positioned perpendicular to the axis of the implant. These sections were polished to a thickness of 30–50 mm using a grinding–sliding machine (Microgrinding MG-4000, Exact-Apparatebau, Norderstedt, Germany) and then stained with Stevenel's blue and Van Gieson's picrofuchsin [24]. A thorough microscopic analysis was performed on histological slides using a transmitted light microscope (model Eclipse 80i, Nikon, Tokyo, Japan) combined with a digital camera (Nikon model DS-5M-L1). Other sections were polished with diamond paper and sputter-coated with carbon for SEM studies.

3. Results

3.1. In vitro evaluation

3.1.1. Surface structures

The EDX results showed that: (1) 3.8–5.3 at.% Na was incorporated on the surface on NaOH treatment; (2) the incorporated Na was completely replaced with Ca on subsequent $CaCl_2$ treatment; (3) the amount of Ca incorporated (4.1–5.9 at.%) remained almost unchanged after subsequent heat and water treatments (3.7–5.2 at.%). Similar tendencies were observed in our previous studies on ACaH600W-treated cp-Ti [19] and Ti15Zr4Nb4Ta [17]. The amount of Ca incorporated did not differ between the ACaH600W- and ACaH700W-treated samples.

Fig. 2 shows FE-SEM photographs of the surfaces of the treated implants. A fine network structure was seen at the nanometer scale on all treated samples, although the alloy plates exhibited a finer network structure than the cp-Ti plate.

3.1.2. Apatite formation

Fig. 3 shows FE-SEM photographs of the surfaces of the treated implants that were soaked in SBF for 1 day. The amount of apatite deposited on the ACaH700W-treated implants increased so that the apatite deposits covered almost the entire surface within 1 day of soaking in SBF. However, the apatite deposits on the surface of the ACaH600W-treated Ti15Zr4Ta4Nb implants only partially covered the surface after 1 day, although they extended to cover the entire surface within 3 days of soaking in SBF.

3.2. In vivo evaluation

All rabbits tolerated the surgical procedure well. None exhibited infection of the surgical site, dislocation of the implants, or adverse reactions such as inflammation or foreign body reactions on or around the implants.

3.2.1. Detachment test (failure load)

Some of the untreated implants were detached from bone prior to testing and were assigned a failure load of 0 N. As seen in Fig. 4, the untreated plates showed a slight increase in failure load throughout the experimental period. In contrast, at all time periods the ACaH700W- and ACaH600W-treated groups both showed significantly higher bonding strength than the untreated groups ($P < 0.001$). Among the cp-Ti and Ti15Zr4Ta4Nb plates the ACaH700W-treated samples showed significantly higher bonding strength than the ACaH600W-treated samples at all time periods.

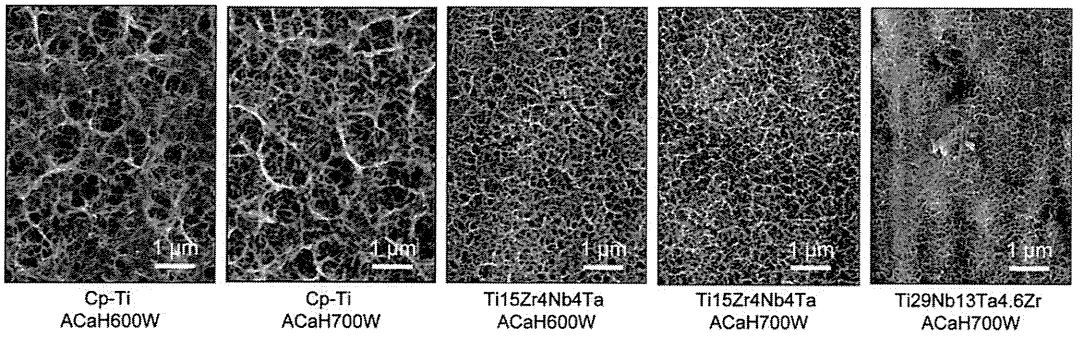

Fig. 2. FE-SEM photographs of the surfaces of the treated implants.

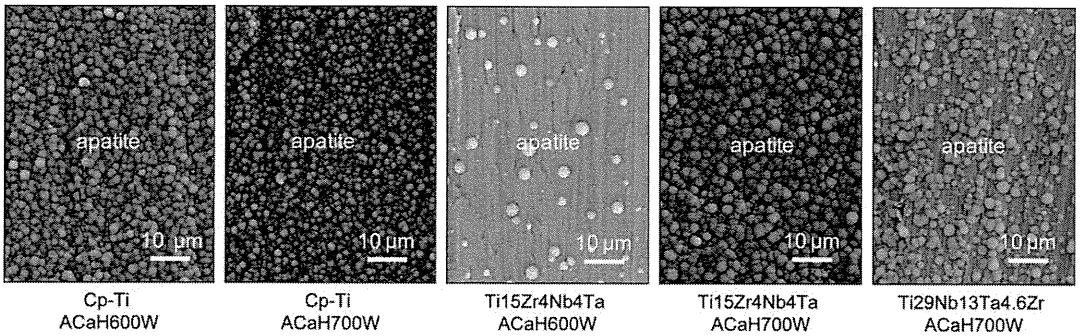

Fig. 3. FE-SEM photographs of the surfaces of the treated implants soaked in SBF for 1 day.

The failure load for all treated groups increased steadily with time. At 4 weeks Ti29Nb13Ta4.6Zr showed a significantly lower bonding strength than cp-Ti and Ti15Zr4Ta4Nb after ACaH700W treatment. Furthermore, from 8 to 26 weeks cp-Ti showed a significantly higher bonding strength than the others after ACaH700W treatment.

3.2.2. Histological examination

3.2.2.1. Surface examination after detachment test. After the detachment tests a bone residue was observed on the intact surface layer of the treated plates in SEM images taken at all time intervals. We could easily distinguish the bony area from the bare metal surface because the average Ca:P ratio in the bony area was 1.66 according to SEM–EDX analysis. In the images taken at 4 weeks there was little bone residue on all untreated plates. In addition, the untreated plates showed almost no increase in bone residue throughout the experimental period. In contrast, some bone residue was observed on the treated plates at 4 weeks, and the amount of residue increased with time. Mature bone was well integrated on the treated plates at all time periods. No significant difference was observed among the ACaH600W- and ACaH700W-treated samples. At 26 weeks, we observed abundant integration of mature bone on the entire treated plate, no surface breakage, and a rupture surface on the bone side for all samples (Fig. 5). Consistent with this finding, in the observations of the bony surface after the detachment testTi was not observed and was not detected by EDX in any sample, indicating that the treated surface structure is sufficiently strong.

3.2.2.2. Interface examination. No inflammatory reactions or adverse effects were observed at the bone–implant interface in all samples subjected to SEM imaging (backscattered mode) and surface staining with Stevenel's blue and Van Gieson's picrofuchsin.

1. At 4 weeks in the untreated group, although immature bone approached the implant, it did not directly bond with the implant, thereby giving rise to a gap between the implant and bone (Fig. 6A). The treated samples, however, all exhibited direct bone–implant bonding, at least partially. However, the bone at the interface was not completely mature in all the implants because of the absence of a laminar structure (Fig. 6). In the stained untreated implant group (Fig. 7A) a little bone formation was found in a transverse direction; the observed bone tissue was of an irregular form without a parallel fibered pattern. In the treated alloy implants newly formed bone bridged the gap, but was coarse and irregular (Fig. 7B, 7C, 7E and 7F). The ACaH700 W-treated cp-Ti implants (Fig. 7D), however, exhibited a bone–Ti interface relatively filled with parallel fibered lamellar bone and bone marrow. Furthermore, the ACaH700W-treated cp-Ti plates had an unclear boundary between new bone and original bone, which indicated bone maturity.
2. At 8 weeks the untreated plates still had a thin layer of intervening fibrous tissue at the interface. However, the treated plates exhibited cortical bone that seemed to extend over the plate. The contact length between cortical bone and implant was wider than that at 4 weeks. Almost complete direct bone bonding was observed in all treated implants.
3. At 16 and 26 weeks the untreated plates still had a thin fibrous tissue layer at the interface or only made partial direct contact with bone (Fig. 8A). Some untreated implants became detached from the bone during cutting, grinding, and staining, which indicated relatively weak bonding. In contrast, the treated samples showed direct bonding with bone and no intervening soft tissue. In particular, the ACaH700W-treated samples exhibited new bone of such maturity that the new bone was undistinguishable from the original bone (Fig. 8D–F), although this was not the case with the ACaH600W-treated plates (Fig. 8B

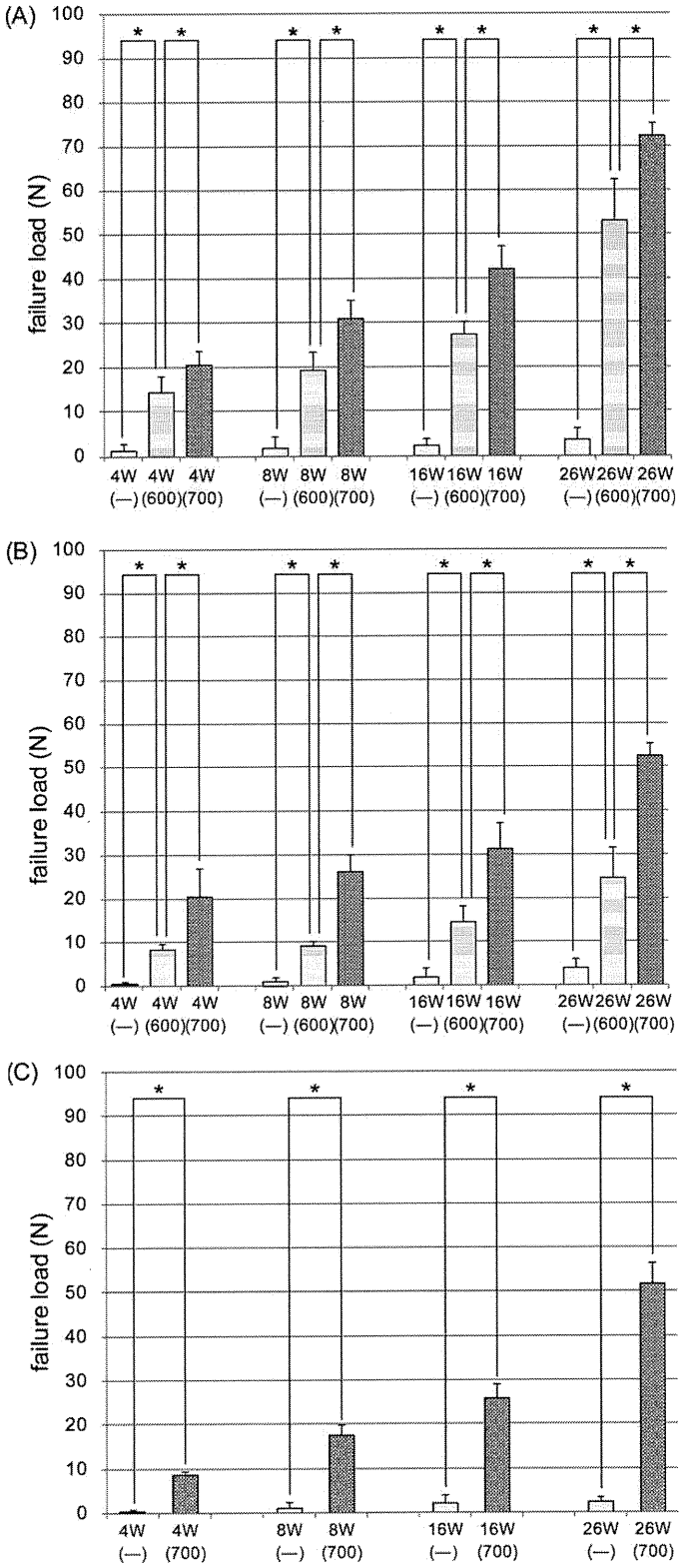

Fig. 4. The results of the detachment test. (A) cp-Ti plates. (B) Ti15Zr4Ta4Nb plates. (C) Ti29Nb13Ta4.6Zr plates. —, Untreated plates; 600, ACaH600W treatment; 700, ACaH700W treatment. The error bars represent standard deviations. * A significant difference.

and 8C). Over time the amount of bone directly bonded to the implant increased, and the directly bonded bone matured and was converted to lamellar bone (Fig. 8B–F).

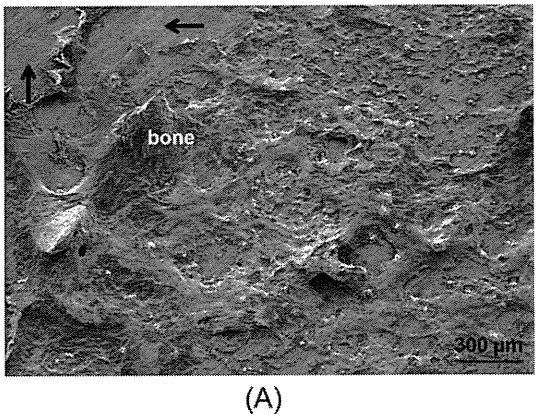

Fig. 5. SEM image of the surface of ACaH700W-treated cp-Ti implants after the detachment test at 26 weeks. Mature bone was well integrated onto the treatment layer. No surface breakage was observed (arrow).

4. Discussion

The results show that all ACaHW-treated implants successfully bonded to bone and retained this bond for up to 26 weeks. In contrast, the untreated implants showed almost no bonding until 8 weeks, and only slight bonding after 16 weeks. Histological examination confirmed that the newly formed bone tissue almost made direct contact with the treated implants as early as 4 weeks after surgery. Conversely, in the untreated implants a layer of fibrous tissue existed at the bone–implant interface 8 weeks after surgery, and bone tissue made only partial contact with the implant at 16 and 26 weeks. These results confirm that ACaHW treatment enhanced bone bonding.

In the present study, cp-Ti showed a relatively higher bonding strength than Ti alloys after ACaHW treatment. The reasons for the differences in bonding strength between ACaHW-treated cp-Ti and Ti alloys are not clear. The bonding strength of the treated substrate is influenced by many factors, such as strength of the substrate and thickness and strength of the treated layers [25]. In general, a thicker calcium titanate layer causes earlier apatite formation and combines with bone earlier than a thin calcium titanate layer. The thickness of the treated layer on cp-Ti and Ti–Zr–Nb–Ta alloys are reported as approximately 1 and 0.5 μm, respectively [17]. This difference may have more impact on the bonding strength than the strength of the substrate.

Ti15Zr4Nb4Ta and Ti29Nb13Ta4.6Zr have been reported to show better biocompatibility than Ti6Al4V [14,16,26,27]. Furthermore, although living bone seems to come close to the surface of these alloys, these bioinert materials do not exhibit osteoconductivity. Recently many researchers have attempted to make these alloys more bioactive, and a few have succeeded [1,2]. Sugino demonstrated apatite formation in vitro on Ti15Zr4Nb4Ta implants subjected to thermal oxidation at 500 °C after machining macrogrooves with widths of 500 μm on the implant surface [1]. Kasuga reported a method for applying a coating of bioactive calcium phosphate invert glass on Ti29Nb13Ta4.6Zr, and showed that the tensile bond between the substrate and coating layer was of high strength [2]. However, these methods cannot be used to treat the entire surface of complex porous implants because of limited apatite formation in the internal surfaces of microgrooves [1] and difficulties encountered with uniform entry of the pulverized glass slurry into the complex microstructure due to its viscous nature [2]. In contrast, our simple method that involves chemical and heat treatment using aqueous solutions and subsequent heat treatment can be used to uniformly treat the entire surface of porous implants having any type of complicated structure. However, our

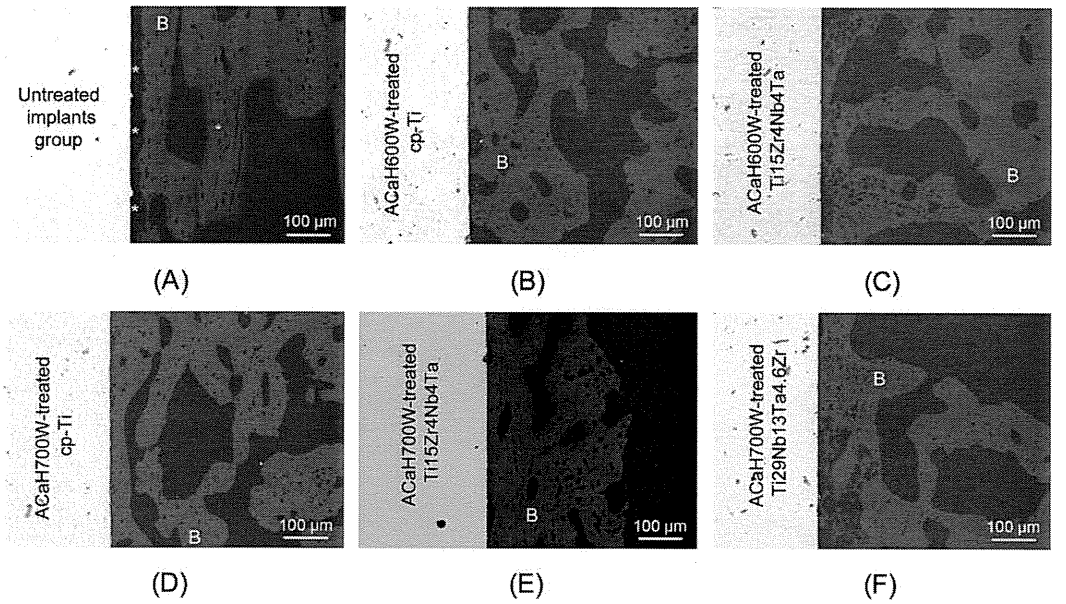

Fig. 6. SEM image (obtained in backscattered mode) of the implant–bone interface at 4 weeks. (A) Untreated implant group. Although immature bone approached the implant, it did not directly bond with the implant, giving rise to a gap (white asterisks) between the implant and the bone. (B) ACaH600W-treated cp-Ti plates. (C) ACaH600W-treated Ti15Zr4Nb4Ta plates. (D) ACaH700W-treated cp-Ti plates. (E) ACaH700W-treated Ti15Zr4Nb4Ta plates. (F) ACaH700W-treated Ti29Nb13Ta4.6Zr plates. Direct bonding between bone and implant was observed for all treated implants. The contact area was comparatively large (D, E) and the new bone was relatively mature and dense. B, bone.

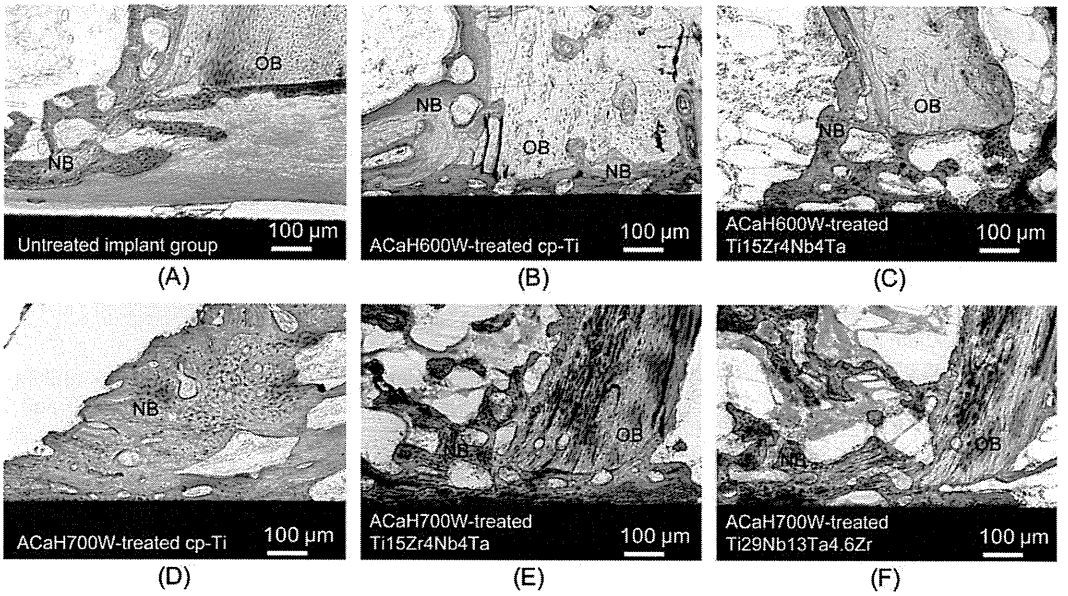

Fig. 7. Surface staining of the bone–implant interface with Stevenel's blue and Van Gieson's picrofuchsin at 4 weeks. (A) Untreated implant group. (B) ACaH600W-treated cp-Ti plates. (C) ACaH600W-treated Ti15Zr4Nb4Ta plates. (D) ACaH700W-treated cp-Ti plates. (E) ACaH700W-treated Ti15Zr4Nb4Ta plates. (F) ACaH700W-treated Ti29Nb13Ta4.6Zr plates. Both the treated and untreated implant groups showed coarse bone formation on the implant. The treated implants (B–F) showed partial direct bone bonding, whereas the untreated implant (A) showed a thick layer of intervening fibrous tissue. The ACaH700W-treated cp-Ti plates (D) had an unclear boundary between the new bone and original bone, which indicated bone maturity. OB, original bone; NB, new bone.

conventional alkali and heat treatment, although successful with Al- and V-containing Ti alloys (Ti6Al4V, Ti15Mo5Zr3Al, and Ti6Al2Nb1Ta) [9–11], was ineffective with Ti15Zr4Nb4Ta and Ti29Nb13Ta4.6Zr.

The increased apatite formation after the NaOH and heat treatments is attributed to the formation of sodium titanate on the surface. In SBF sodium titanate releases Na^+ ions via exchange with H_3O^+ ions to form Ti–OH groups on the surface, which induce apatite formation, as earlier described for NaOH- and heat-treated Ti metal [28,29]. However, Ti containing Ca^{2+} ions instead of Na^+ ions on its surface is expected to exhibit higher apatite formation, since the released Ca^{2+} ions more effectively increase the ionic activity product of the apatite in the surrounding body fluids [30]. In fact, several studies have investigated the incorporation of Ca^{2+} ions onto Ti surfaces [31–33]. However, the techniques mentioned in these studies require expensive specialized apparatus for ion implantation [32] or a specialized high pressure apparatus operating in an aqueous environment at high temperatures for application to medical devices [31,33]. We recently ascertained the in vitro apatite forming ability of cp-Ti, Ti15Zr4Nb4Ta, and

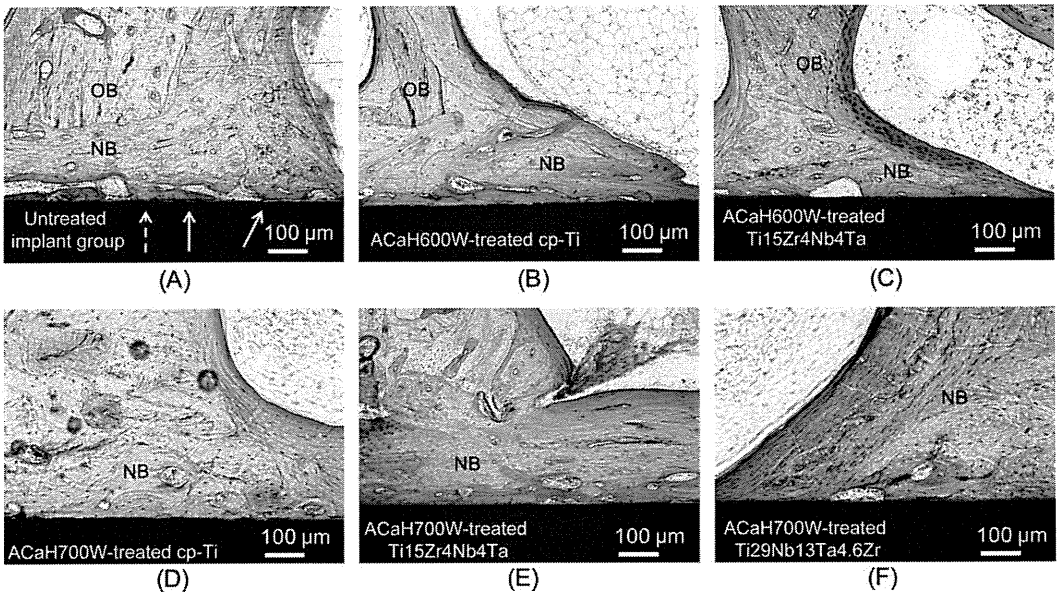

Fig. 8. Surface staining of the bone–implant interface with Stevenel's blue and Van Gieson's picrofuchsin at 16 weeks. (A) Untreated implant group. (B) ACaH600W-treated cp-Ti plates. (C) ACaH600W-treated Ti15Zr4Nb4Ta plates. (D) ACaH700W-treated cp-Ti plates. (E) ACaH700W-treated Ti15Zr4Nb4Ta plates. (F) ACaH700W-treated Ti29Nb13Ta4.6Zr plates. Both the treated and untreated implant groups showed mature bone on the implant. The treated implants (B–F) showed almost complete direct bone bonding, whereas the untreated implant (A) showed a thin layer of intervening fibrous tissue (white arrow) and only partial direct bone bonding (dotted white arrow). The ACaH700W-treated samples exhibited new bone of such maturity that the new bone was undistinguishable from the original bone (D–F), although this was not the case with the ACaH600W-treated plates (B, C). OB, original bone; NB, new bone.

Ti29Nb13Ta4.6Zr alloy implants by using simple and economical ACaHW treatments [17–19]. Furthermore, in the present study an in vivo bone bonding ability was confirmed. The mechanisms of apatite formation following ACaHW treatment are interpreted in terms of surface structural changes as follows. The apatite forming ability increased after $CaCl_2$ treatment following NaOH treatment, although this ability is lost after heat treatment to strengthen the treated layer due to the reduced mobility of Ca^{2+} ions in calcium titanate [17]. This problem is resolved by the subsequent water treatment, which contributes to increased mobility of the Ca^{2+} ions in calcium titanate by incorporation of H_3O^+ ions [17].

We previously reported that sodium removal through hot water immersion in the course of alkali and heat treatment considerably enhanced the apatite forming ability of Ti in SBF. Sodium removal enhanced the bone bonding strength of Ti subjected to alkali and heat treatment at 4 and 8 weeks post-operative, however, the failure loads of the implants subjected to sodium-free alkali and heat treatment decreased after 16 weeks implantation because the treated layer flaked off [5]. On the other hand, the failure loads in the present study did not decrease and no flaking of the treated layer was observed by SEM through to the end. We considered that the stability of the ACaHW-treated layer was confirmed by these results.

In comparison with the case of heat treatment at 600 °C, heat treatment at 700 °C led to a significant improvement in apatite formation in SBF and tensile strength in vivo. However, the EDX results were not significantly different. In the detachment test all treated specimens ruptured on the bone side. Hence, we consider that the differences in failure load between samples subjected to ACaH600W and ACaH700W treatment stem from bone maturity and adhesion based on the histological findings. In other words, the increase in heat treatment temperature to 700 °C increased the extent of bone formation around the implant.

In general, the apatite forming ability of Ti metal subjected to alkali and heat treatment was liable to decrease when the treated Ti metal was stored in a humid environment for a long period of time, because of the release of Na^+ ions from the sodium titanate. However, it is reported that the apatite forming ability of ACaHW-treated Ti metal did not decrease, even when the treated Ti metal was kept in a humid environment [19]; this finding can be attributed to the low mobility of Ca^{2+} ions compared with Na^+ ions in the titanate.

Thus, from an overall perspective, it is expected that when Ti15Zr4Ta4Nb and Ti29Nb13Ta4.6Zr alloys with superior biocompatibility and mechanical properties are endowed with bioactivity and stability through ACaHW treatment, the treated alloys will be useful in developing novel orthopedic implants that function under loaded conditions, such as cementless joint replacement implants, external fixation pins, and spinal fusion implants.

5. Conclusions

Commercially pure Ti and its Zr-, Nb-, and Ta-containing alloys (without V and Al), namely Ti15Zr4Ta4Nb and Ti29Nb13Ta4.6Zr, exhibit enhanced apatite formation in vitro and bone bonding in vivo after alkali, $CaCl_2$, heat, and water treatment. In particular, implants heat treated at 700 °C have significantly augmented apatite formation in SBF and stronger bone bonding in vivo. The present results suggest that these treated Ti alloys may be useful to develop novel orthopedic implants that function under loaded conditions, because of their superior mechanical properties and excellent bioactivity and cytocompatibility.

Acknowledgements

This work was supported by the Translational Research Promotion Project as part of the Health Assurance Program of the New Energy and Industrial Technology Development Organization (NEDO). We thank Dr. Yoshimitsu Okazaki for supplying the alloy used in the study.

Appendix Appendix. A. Figures with essential colour discrimination

Certain figures in this article, particularly Figs. 1, 7, and 8 are difficult to interpret in black and white. The full colour images

can be found in the on-line version, at doi:10.1016/j.actbio.2010.09.026.

References

[1] Sugino A, Ohtsuki C, Tsuru K, Hayakawa S, Nakano T, Okazaki Y, et al. Effect of spatial design and thermal oxidation on apatite formation on Ti–15Zr–4Ta–4Nb alloy. Acta Biomater 2009;5:298–304.

[2] Kasuga T, Nogami M, Niinomi M, Hattori T. Bioactive calcium phosphate invert glass-ceramic coating on beta-type Ti–29Nb–13Ta–4.6Zr alloy. Biomaterials 2003;24:283–90.

[3] De Groot K, Geesink R, Klein C, Serekian R. Plasma sprayed coatings of hydroxyapatite. J Biomed Mater Res 1987;21:1375–81.

[4] Klein CP, Patka P, van der Lubbe HB, Wolke JG, de Groot K. Plasma-sprayed coatings of tetracalciumphosphate, hydroxyl-apatite, and alpha-TCP on titanium alloy: an interface study. J Biomed Mater Res 1991;25:53–65.

[5] Fujibayashi S, Nakamura T, Nishiguchi S, Tamura J, Uchida M, Kim HM, et al. Bioactive titanium: effect of sodium removal on the bone-bonding ability of bioactive titanium prepared by alkali and heat treatment. J Biomed Mater Res 2001;56:562–70.

[6] Takemoto M, Fujibayashi S, Neo M, Suzuki J, Kokubo T, Nakamura T. Mechanical properties and osteoconductivity of porous bioactive titanium. Biomaterials 2005;26:6014–23.

[7] Takemoto M, Fujibayashi S, Neo M, Suzuki J, Matsushita T, Kokubo T, et al. Osteoinductive porous titanium implants: effect of sodium removal by dilute HCl treatment. Biomaterials 2006;27:2682–91.

[8] Kawanabe K, Ise K, Goto K, Akiyama H, Nakamura T, Kaneuji A, et al. A new cementless total hip arthroplasty with bioactive titanium porous-coating by alkaline and heat treatment: average 4.8-year results. J Biomed Mater Res B Appl Biomater 2009;90:476–81.

[9] Kim HM, Miyaji F, Kokubo T, Nakamura T. Preparation of bioactive Ti and its alloys via simple chemical surface treatment. J Biomed Mater Res 1996;32:409–17.

[10] Nishiguchi S, Kato H, Fujita H, Kim HM, Miyaji F, Kokubo T, et al. Enhancement of bone-bonding strengths of titanium alloy implants by alkali and heat treatments. J Biomed Mater Res 1999;48:689–96.

[11] Kim HM, Takadama H, Kokubo T, Nishiguchi S, Nakamura T. Formation of a bioactive graded surface structure on Ti–15Mo–5Zr–3Al alloy by chemical treatment. Biomaterials 2000;21:353–8.

[12] Steinemann S. Corrosion of Surgical Implants – In Vivo and In Vitro Tests. New York: Wiley; 1980.

[13] Hallab NJ, Vermes C, Messina C, Roebuck KA, Glant TT, Jacobs JJ. Concentration- and composition-dependent effects of metal ions on human MG-63 osteoblasts. J Biomed Mater Res 2002;60:420–33.

[14] Niinomi M. Metallic biomaterials. J Artif Organs 2008;11:105–10.

[15] Okazaki Y, Rao S, Ito Y, Tateishi T. Corrosion resistance, mechanical properties, corrosion fatigue strength and cytocompatibility of new Ti alloys without Al and V. Biomaterials 1998;19:1197–215.

[16] Niinomi M. Fatigue performance and cyto-toxicity of low rigidity titanium alloy, Ti–29Nb–13Ta–4.6Zr. Biomaterials 2003;24:2673–83.

[17] Yamaguchi S, Takadama H, Matsushita T, Nakamura T, Kokubo T. Apatite-forming ability of Ti–15Zr–4Nb–4Ta alloy induced by calcium solution treatment. J Mater Sci Mater Med, 2009.

[18] Yamaguchi S, Kizuki T, Takadama H, Matsushita T, Kokubo T, Fukuda A, et al. Preparation of Bioactive Ti–Nb–Ta–Zr Alloy by Chemical Treatment. Aichi: Japanese Society of Orthopaedic Ceramic Implants; 2009.

[19] Kizuki T, Takadama H, Matsushita T, Nakamura T, Kokubo T. Preparation of bioactive Ti metal surface enriched with calcium ions by chemical treatment. Acta Biomater 2010.

[20] Fujibayashi S, Neo M, Kim HM, Kokubo T, Nakamura T. A comparative study between in vivo bone ingrowth and in vitro apatite formation on Na_2O–CaO–SiO_2 glasses. Biomaterials 2003;24:1349–56.

[21] Nakamura T, Yamamuro T, Higashi S, Kokubo T, Itoo S. A new glass-ceramic for bone replacement: evaluation of its bonding to bone tissue. J Biomed Mater Res 1985;19:685–98.

[22] Kokubo T, Takadama H. How useful is SBF in predicting in vivo bone bioactivity? Biomaterials 2006;27:2907–15.

[23] Onishi E, Fujibayashi S, Takemoto M, Neo M, Maruyama T, Kokubo T, et al. Enhancement of bone-bonding ability of bioactive titanium by prostaglandin E_2 receptor selective agonist. Biomaterials 2008;29:877–83.

[24] Maniatopoulos C, Rodriguez A, Deporter DA, Melcher AH. An improved method for preparing histological sections of metallic implants. Int J Oral Maxillofac Implants 1986;1:31–7.

[25] Takemoto M, Nakamura T. Osteoconduction and its evaluation. In: Kokubo T, editor. Bioceramics and their Clinical Applications. Cambridge: Woodhead Publishing; 2008. p. 183–98.

[26] Okazaki Y, Nishimura E, Nakada H, Kobayashi K. Surface analysis of Ti–15Zr–4Ta alloy after implantation in rat tibia. Biomaterials 2001;22:599–607.

[27] Sumitomo N, Noritake K, Hattori T, Morikawa K, Niwa S, Sato K, et al. Experiment study on fracture fixation with low rigidity titanium alloy: plate fixation of tibia fracture model in rabbit. J Mater Sci Mater Med 2008;19:1581–6.

[28] Takadama H, Kim HM, Kokubo T, Nakamura T. An X-ray photoelectron spectroscopy study of the process of apatite formation on bioactive titanium metal. J Biomed Mater Res 2001;55:185–93.

[29] Takadama H, Kim HM, Kokubo T, Nakamura T. TEM–EDX study of mechanism of bonelike apatite formation on bioactive titanium metal in simulated body fluid. J Biomed Mater Res 2001;57:441–8.

[30] Ohtsuki C, Kokubo T, Yamamuro T. Mechanism of apatite formation on CaO–SiO_2–P_2O_5 glasses in a simulated body fluid. J Non-Cryst Solids 1992;143:84–92.

[31] Chen XB, Li YC, Du Plessis J, Hodgson PD, Wen C. Influence of calcium ion deposition on apatite-inducing ability of porous titanium for biomedical applications. Acta Biomater 2009;5:1808–20.

[32] Nayab SN, Jones FH, Olsen I. Effects of calcium ion implantation on human bone cell interaction with titanium. Biomaterials 2005;26:4717–27.

[33] Park JW, Park KB, Suh JY. Effects of calcium ion incorporation on bone healing of Ti6Al4V alloy implants in rabbit tibiae. Biomaterials 2007;28:3306–13.

Preparation of bioactive Ti-15Zr-4Nb-4Ta alloy from HCl and heat treatments after an NaOH treatment

Seiji Yamaguchi,[1] Hiroaki Takadama,[1] Tomiharu Matsushita,[1] Takashi Nakamura,[2] Tadashi Kokubo[1]

[1]Department of Biomedical Sciences, College of Life and Health Sciences, Chubu University, 1200 Matsumoto-cho, Kasugai-city, Aichi 487-8501, Japan

[2]Department of Orthopaedic Surgery, Graduate School of Medicine, Kyoto University, Kawaharacho54, Shogoin, Sakyo-ku, Kyoto 606-8507, Japan

Received 4 October 2010; revised 2 December 2010; accepted 17 December 2010
Published online 2 March 2011 in Wiley Online Library (wileyonlinelibrary.com). DOI: 10.1002/jbm.a.33036

Abstract: Ti-15Zr-4Nb-4Ta alloy does not contain any cytotoxic elements and has a high mechanical strength. Water or HCl and heat treatments were applied to this alloy after NaOH treatment to form a bioactive titanium oxide layer with a nanometer scale roughness on its surface. The nanometer scale roughness was formed on the surface after the first NaOH treatment and remained, even after a subsequent water or HCl and heat treatment. A layer that was mainly composed of anatase was formed on the surface after the heat treatment. Thus, the treated alloy showed a high apatite-forming ability in an SBF, as well as a high scratch resistance. Its high apatite-forming ability was attributed to its positive surface charge. The same alloy subjected to a heat treatment without a water or HCl treatment after the NaOH treatment did not show an apatite-forming ability. This was attributed to a too slow release rate of sodium ions from the surface in an SBF. Ti-15Zr-4Nb-4Ta alloy samples subjected to a water or HCl and heat treatment after the NaOH treatment are expected to be useful as orthopedic and dental implants, since they can form an apatite layer on their surface in a living body and bond to living bone through this apatite layer. © 2011 Wiley Periodicals, Inc. J Biomed Mater Res Part A: 97A: 135–144, 2011.

Key Words: Ti-15Zr-4Nb-4Ta alloy, acid, positive charge, apatite, cytotoxic-free

INTRODUCTION

Because of their high mechanical strength and good biocompatibility, titanium (Ti) metal and its alloys are widely used in various implants, such as in artificial joints and tooth roots in orthopedic surgery and dentistry. However, they do not bond to living bone, and hence, their fixation to the surrounding bone is not stable for a long period. It has been reported that Ti metal with a surface sodium titanate layer formed after an NaOH and heat treatment forms a bonelike apatite layer on its surface in the living body, and bonds to living bone through this apatite layer.[1–4] This type of chemical and heat treatment has been applied to the porous titanium metal surface layer of an artificial total hip joint, and has been used clinically in Japan since 2007.[5]

The above treatment is effective for inducing bone-bonding bioactivity in conventional Ti-based alloys, such as Ti-6Al-4V,[6] Ti-15Mo-5Zr-3Al,[7] and Ti-6Al-2Nb-1Ta.[2] However, these treatments are not effective in inducing apatite-forming ability in the new Ti-Zr-Nb-Ta alloys,[8] which are free from elements suspected of cytotoxicity. Among these alloys, Ti-15Zr-4Nb-4Ta (Ti-15-4-4) alloy shows a high mechanical strength.[9]

We have previously shown that if this alloy is subjected to NaOH, $CaCl_2$, heat, and water treatments, it forms a Ca-deficient calcium titanate on its surface, and exhibits an apatite-forming ability in a body environment.[10] However, metals enriched with sodium or calcium ions on their surfaces tend to release the sodium or calcium ions to some degree via exchange with oxonium ions in a body fluid, increase pH of surrounding environment by consuming the oxonium ions in it, and, therefore, are liable to have an unfavorable effect on living cells, especially in the narrow spaces of a porous body.

On the other hand, recently, it has also been shown that Ti metal bonds to living bone, if it has been subjected to a heat treatment after an acid treatment to form a titanium oxide layer on its surface.[11] It should be noted that thus formed titanium oxide layer does not release any ions into surrounding fluid in body environment. However, there is a difference in the surface topography after the alkaline and acid treatments. The former treatment gives a nanometer scale roughness, whereas the latter treatment gives a micrometer scale roughness. It is assumed that a nanometer scale roughness may be more suitable for the surface of porous Ti metal in terms of its osteoconductivity as well as osteoinductivity,[12] if the layer does not release any ions. A layer of

Correspondence to: S. Yamaguchi; e-mail: sy-esi@isc.chubu.ac.jp
Contract grant sponsor: Translational Research Promotion Project in Health Assurance Program entrusted from the New Energy and Industrial Technology Development Organization (NEDO)

soluble-ion-free bioactive titanium oxide with a nanometer scale roughness may be formed on Ti metal by applying acid and heat treatments after an NaOH treatment. It has already been reported that such a surface layer is formed on Ti metal if it is subjected to an HCl and heat treatment after an NaOH treatment.[13] From animal experiments, it was confirmed that porous Ti metal subjected to the same treatment exhibits osteoconductivity[14] as well as osteoinductivity.[15]

The aim of this study is to investigate the conditions of chemical and heat treatments for producing a surface layer on Ti-15-4-4 alloy that shows high apatite-forming ability in a body environment without giving any ion release in surrounding fluid, and has a nanometer scale roughness which is considered to be effective for osteoinductivity.[15] The factor governing its high apatite-forming ability is discussed from a view point of surface potential of the Ti-15-4-4 alloy subjected to the chemical and heat treatments.

Regarding the formation of a titanium oxide layer having an apatite-forming ability on Ti-15-4-4 alloy, Sugino et al.[16] have already reported that a rutile layer forms on this alloy after a heat treatment at 500°C precipitates apatite in a simulated body fluid (SBF), but only in the internal surfaces of microgrooves. The reason for the formation of apatite is not yet known.

MATERIALS AND METHODS

Sample and surface treatments

Ti-15-4-4 alloy (Ti = balance, Zr = 14.51, Nb = 3.83, Ta = 3.94, Pd = 0.16, and O = 0.25 mass%) supplied by the Kobelco Research Institute, Inc., Japan, was cut into rectangular-shaped samples with dimensions of 10 × 10 × 1 mm^3, abraded with 400 diamond plates, and washed with acetone, 2-propanol, and ultrapure water in an ultrasonic cleaner for a period of 30 min, and then dried at 40°C. The samples were soaked in 5 mL of a 5*M* NaOH aqueous solution at 60°C for a period of 24 h in an oil bath, and then shaken at a speed of 120 strokes/min. After being removed from the solution, the alloy samples were gently rinsed with ultrapure water for a period of 30 s, and dried at 40°C. The samples were subsequently soaked in 10 mLof a dilute HCl solution at a concentration of 0.5 or 50 m*M* at 40°C for a period of 24 h. The HCl treatment using a 0.5 or 50 m*M* HCl solution is denoted in the manuscript as a 0.5 HCl or 50 HCl treatment, respectively. For reference, the alloy sample was soaked in 200 mL of ultrapure water at 40°C for a period of 24 h after the NaOH treatment, where the ultrapure water was refreshed after a period of 12 h. The alloy samples were then removed from the solution, washed with ultrapure water, and then dried. After the chemical treatment, they were heated to 600°C at a rate of 5°C/min in a Fe-Cr electrical furnace in air, kept at 600°C for a period of 1 h, and then allowed to cool at the natural rate of the furnace.

Soaking in an SBF

The samples subjected to chemical and heat treatments were soaked at 36.5°C in 24 mL of a simulated body fluid (SBF)[17] having ion concentrations nearly equal to those of human blood plasma (Na^+ = 142.0, K^+ = 5.0, Ca^{2+} = 2.5, Mg^{2+} = 1.5, Cl^- = 147.8, HCO_3^- = 4.2, HPO_4^{2-} = 1.0, and SO_4^{2-} = 0.5 m*M*). The SBF was prepared by dissolving reagent-grade NaCl, $NaHCO_3$, KCl, $K_2HPO_4{\cdot}3H_2O$, $MgCl{\cdot}6H_2O$, $CaCl_2$, and Na_2SO_4 (Nacalai Tesque, Inc., Kyoto, Japan) in ultrapure water and buffed at pH = 7.4 with tris hydroxymethylaminomethane $(CH_2OH)_3CNH_2$ (Nacalai Tesque, Inc., Kyoto, Japan), and 1*M* HCl at 36.5°C. After soaking in the SBF for 3 d, the samples were removed from the SBF, gently rinsed with ultrapure water and dried at 40°C.

Surface analysis

Scanning electron microscopy. The surface and cross-sectional area of the alloy samples subjected to chemical and heat treatments, and those subsequently soaked in an SBF were coated with a Pt/Pd film and observed under a field-emission scanning electron microscope (FE-SEM; S-4300, Hitachi Co., Japan) using an acceleration voltage of 15 kV. The sample preparation for the cross-sectional observations followed the procedure given in our previous article.[18]

Thin film X-ray diffraction and Fourier-transform confocal laser Raman spectroscopy. The surface of the alloy samples subjected to the chemical and heat treatments, and those subsequently soaked in an SBF were analyzed using thin film X-ray diffraction (TF-XRD, Model RNT-2500, Rigaku Co., Japan) and Fourier transform confocal laser Raman spectroscopy (FT-Raman, LabRAM HR800, Horiba Jobin-Yvon, France). The TF-XRD used a CuKα X-ray source operating at 50 kV and 200 mA, and the glancing angle of the incident beam was set to an angle of 1° against the sample surface. The FT-Raman used an argon laser with a wavelength of 514.5 nm as the laser source.

Scratch resistance measurements. The scratch resistance of the surface layer formed on the alloy samples from the chemical and heat treatments was measured using a thin film scratch tester (Model CSR-2000, Rhesca Co., Japan), employing a stylus with a diameter of 5 μm with a spring constant of 200 g/mm. Based on the data in the JIS R-3255 standard, the amplitude, scratch speed, and loading rate used were 100 μm, 10 μm/s, and 100 mN/min, respectively. Five measurements were carried out for each sample, and the average value was used in our analysis.

Zeta potential measurements. Large size Ti-15-4-4 plates (dimensions = 13 × 33 × 1 mm^3) were prepared for the zeta potential measurements using the method of chemical and heat treatments described in Sample and surface treatments, where only the volumes of the solutions were increased to 15 mL for the NaOH solution, 600 mL for water, and to 30 mL of the 0.5 HCl or 50 HCl solutions, in accordance with the increase in surface area of the samples. The treated alloy samples were electrically grounded to allow for any leakage of stray charge, and were immediately set in a zeta potential and particle size analyzer (Model ELS-Z1, Otsuka Electronics Co., Japan) using a glass cell for the plate sample. The zeta potential of the samples was

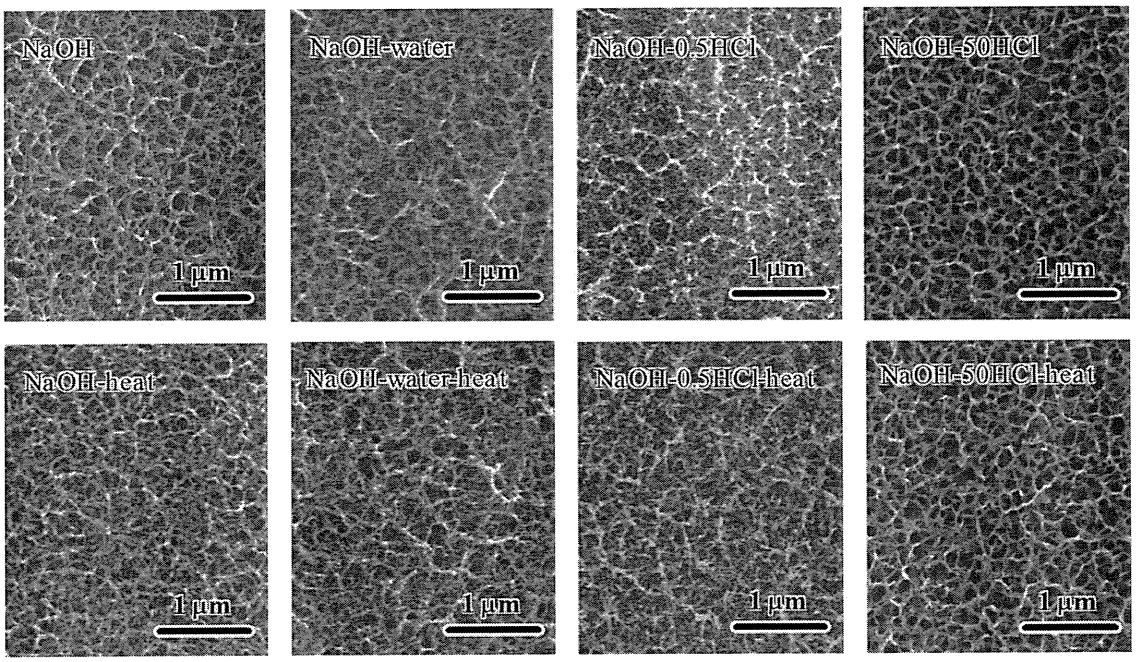

FIGURE 1. FE-SEM photographs of the surfaces of NaOH-treated Ti-15Zr-4Nb-4Ta alloy subsequently subjected to water, 0.5 HCl, or 50 HCl, and heat treatments.

measured under an applied voltage of 40 V in a 50 or 100 m*M* NaCl solution. The dispersant monitoring particles of polystyrene latex (size = 500 nm) were coated with hydroxyl propyl cellulose. Five samples were measured for each experimental condition, and the average value was used in our analysis.

X-ray photoelectron spectroscopy. The surfaces of the alloy samples soaked in the SBF for various periods after the chemical and heat treatments were analyzed using X-ray photoelectron spectroscopy (XPS, ESCA-3300KM, Shimadzu Co., Japan). In our analysis, Mg-Kα radiation ($\lambda = 9.8903$ Å) was used as the X-ray source. The XPS take-off angle was set at 45 degrees, which enabled the system to detect photoelectrons to a depth of 5 to 10 nm from the surface. The binding energy of the measured spectra was calibrated by reference to the C_{1s} peak of the surfactant CH_2 groups on the substrate at 284.6 eV. The measured spectra were decomposed and subjected to curve fitting for quantitative analysis.

RESULTS

Surface structure

Figure 1 shows FE-SEM photographs of the surface of the alloy samples subjected to water, 0.5 HCl or 50 HCl, and heat treatments after an NaOH treatment. A fine network structure on the nanometer scale was formed on the surface of the alloy after the initial NaOH treatment, and this was essentially unchanged by the subsequent chemical and heat treatments.

Figure 2 shows FE-SEM photographs of the cross-section of the samples shown in Figure 1. A 500-nm thick layer, which was composed of many feather-like phases that were elongated perpendicular to the surface, had formed on the surface of the Ti-15-4-4 alloy after the NaOH treatment. The density of the surface layer increased with increasing depth. The thickness of the surface layer was unchanged by the subsequent water or 0.5 HCl treatment, but decreased slightly after the 50 HCl treatment. The subsequent heat treatment did not change the surface structure.

Table I shows the result of the XPS quantitative analysis of the surface of the alloy samples subjected to the NaOH, water, 0.5 HCl, or 50 HCl, and heat treatments. The NaOH treatment incorporated 4.9 atm. % of Na ions into the surface of the alloy samples. The Na ions were completely removed by both the subsequent water and 0.5 HCl or 50 HCl treatment. It should be noted that some of the alloying elements, such as Zr, Nb, and Ta were released by the NaOH treatment, but some remained, even after the subsequent water and 0.5 HCl or 50 HCl treatment. The slight increase in minor alloying elements after the 50HCl treatment reflected the decrease in thickness of the surface layer. When the NaOH-treated sample was heated, the Na content significantly increased to 12.3 atm. %, indicating that the surface layer was densified after the heat treatment after dehydration. The heat treatment induced no apparent changes in the chemical composition for the NaOH-water- and NaOH-0.5 HCl-treated samples, but a slight increase in the Zr, Nb, and Ta contents was detected for the NaOH-50 HCl-treated sample.

Figure 3 shows the TF-XRD and FT-Raman profiles of the surface of the alloy samples subjected to the NaOH, and then a water and 0.5 HCl or 50 HCl treatment. The broad TF-XRD peaks occurring around $2\theta = 24$, 28, and 48

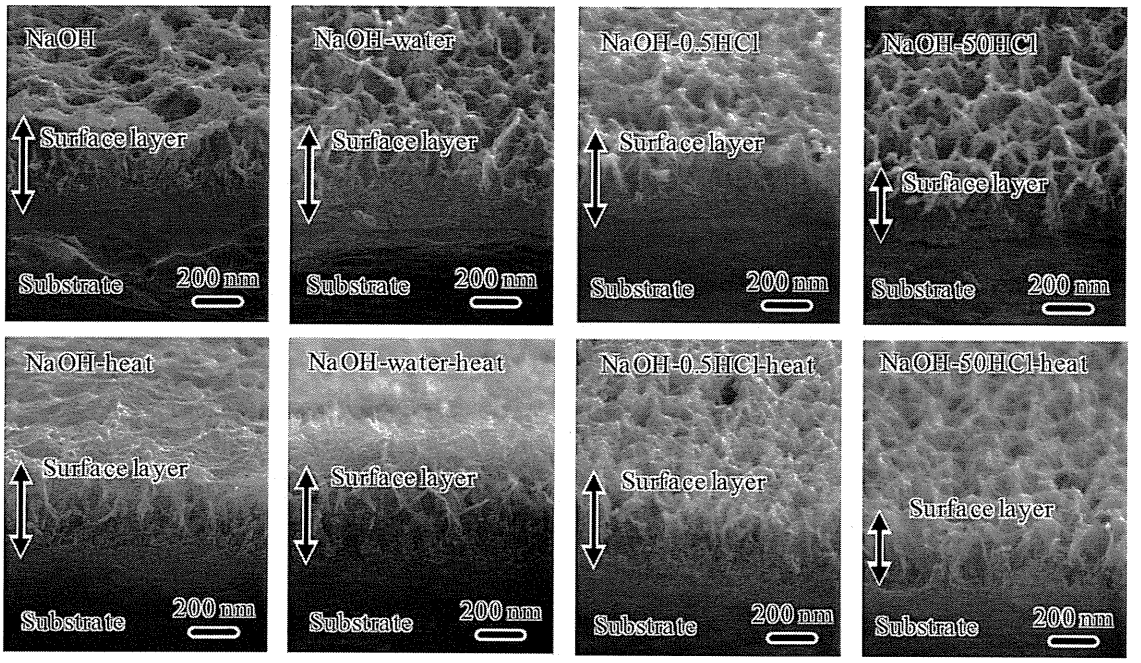

FIGURE 2. FE-SEM micrographs of the cross-sections of NaOH-treated Ti-15Zr-4Nb-4Ta alloy subsequently subjected to water, 0.5 HCl, or 50 HCl, and heat treatments.

degrees and FT-Raman peaks occurring around wavenumbers = 280, 450, 700, 820, and 910 cm^{-1} after the NaOH treatment were assigned to sodium hydrogen titanate ($Na_xH_{2-x}Ti_3O_7$).[19,20] When the NaOH-treated samples were subjected to water and 0.5 HCl or 50 HCl treatments, the intensity of the TF-XRD peak occurring around 2θ = 28 degrees and the Raman peak occurring around wave number = 910 cm^{-1} decreased, indicating that the sodium hydrogen titanate had transformed into hydrogen titanate ($H_2Ti_3O_7$)[19,20] as a result of the exchange of the sodium and oxonium ions.

Figure 4 shows the TF-XRD and FT-Raman profiles of the alloy samples that were subsequently subjected to a heat treatment. When the NaOH-treated sample was subsequently heat treated, the sodium hydrogen titanate layer transformed into sodium titanate ($Na_2Ti_6O_{13}$) accompanied with anatase and rutile phases. On the other hand, when the NaOH-, and the water- and 0.5 HCl- or 50 HCl-treated samples were heat treated, the hydrogen titanate layer was converted to anatase, accompanied by a small amount of rutile.

Figure 5 shows the scratch resistance of the surface of the alloy samples subjected to NaOH, water, 0.5 HCl or 50 HCl, and heat treatments. The scratch resistance of the NaOH-treated sample was as low as 10 m*N*, and was not changed by either a subsequent water or 0.5 HCl or 50 HCl treatment. However, the scratch resistance increased significantly to >90 m*N* after a subsequent heat treatment.

The zeta potential was not able to be measured for the alloy samples subjected to the NaOH, and water and 0.5 HCl or 50 HCl treatments, since their surface was electrically conducting. Figure 6 shows the zeta potential of alloy samples subjected to a heat treatment after an NaOH, and subsequent water and 0.5 HCl or 50 HCl treatment. The alloy samples heat treated after the NaOH treatment showed a negative zeta potential, around −7 mV, whereas samples of

TABLE I. Result of XPS Quantitative Analysis of Surface Layer of Ti-15Zr-4Nb-4Ta Alloy Untreated and Subjected to NaOH, water, 0.5 HCl, or 50 HCl, and Heat Treatments

	Element/atm. %						
Treatment	O	Ti	Na	Zr	Nb	Ta	Pd
Untreated	73.7	21.2	0	3.7	0.9	0.6	0
NaOH	69.6	23.9	4.9	1.1	0.4	0.2	0
NaOH–water	72.1	26.0	0	1.0	0.6	0.4	0
NaOH–0.5 HCl	72.0	26.2	0	0.9	0.6	0.4	0
NaOH–50 HCl	72.9	23.8	0	1.6	1.2	0.4	0
NaOH–heat	63.6	22.4	12.3	0.8	0.8	0.2	0
NaOH–water-heat	72.0	25.3	0	1.1	1.2	0.4	0
NaOH–0.5 HCl-heat	72.0	25.8	0	1.0	0.8	0.4	0
NaOH–50 HCl-heat	72.9	22.3	0	2.3	1.9	0.7	0

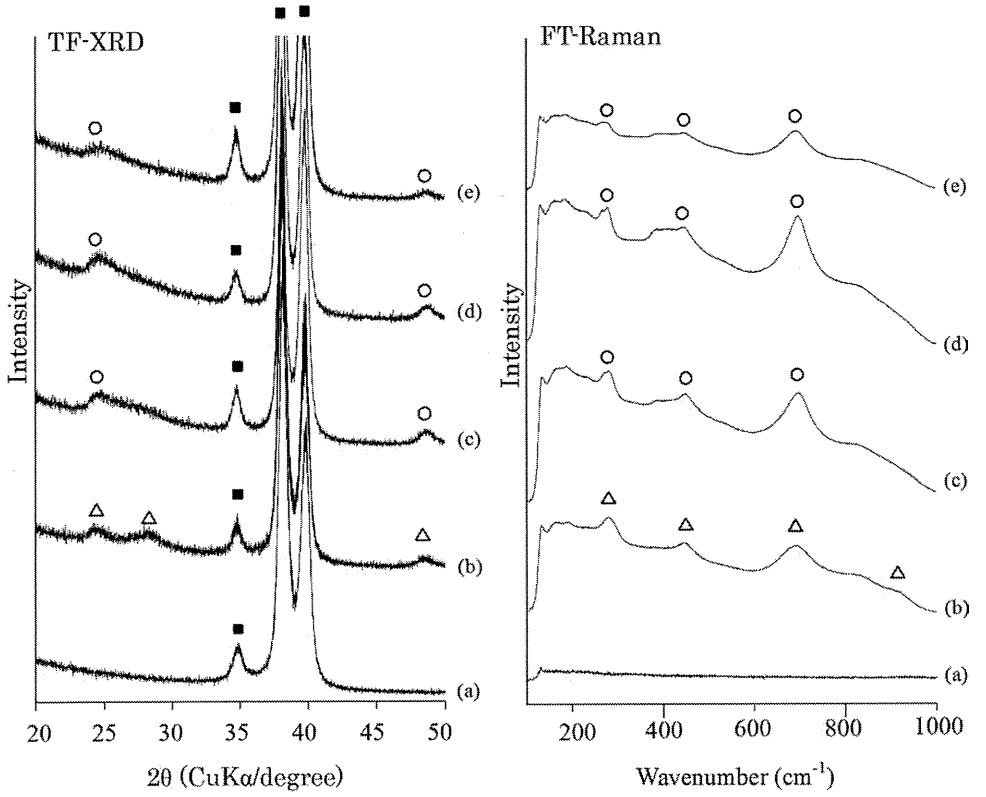

FIGURE 3. TF-XRD and FT-Raman profiles of the surfaces of Ti-15Zr4Nb-4Ta- alloy (a) untreated and subjected to (b) NaOH treatment, (c) NaOH and water treatments, (d) NaOH and 0.5 HCl treatments, and (e) NaOH and 50 HCl treatments. ■, α-Titanium; △, sodium hydrogen titanate ($Na_xH_{2-x}Ti_3O_7$); ○, hydrogen titanate ($Na_xH_{2-x}Ti_3O_7$).

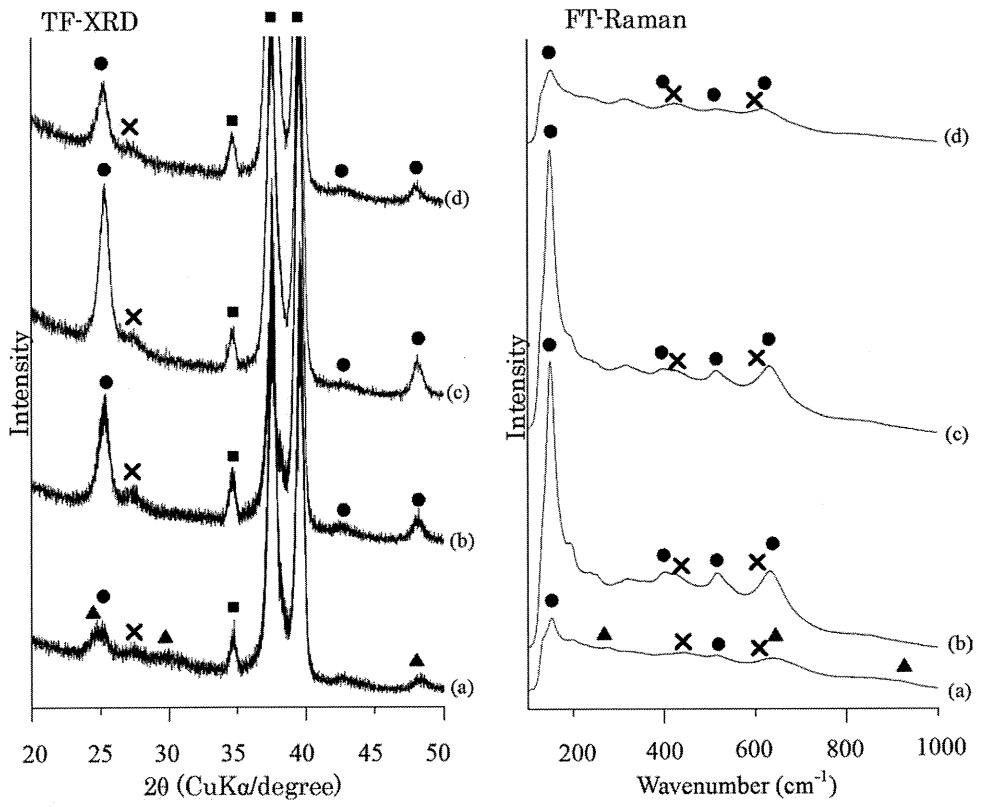

FIGURE 4. TF-XRD and FT-Raman profiles of the surfaces of Ti-15Zr-4Nb-4Ta alloy subjected to (a) NaOH and heat treatments, (b) NaOH, water, and heat treatments, (c) NaOH, 0.5 HCl, and heat treatments, and (d) NaOH, 50 HCl, and heat treatments. ■, α-Titanium; ▲, sodium titanate ($Na_2Ti_6O_{13}$); ●, Anatase; ×, Rutile.